Study of Charmonia near the deconfining transition on the Lattice

Takashi Umeda,

Department of Physics, Faculty of Science, Hiroshima University,
Kagamiyama 1-3-1, Higashi-hiroshima, 739-8526, JAPAN,
E-mail: umeda@hiroh2.hepl.hiroshima-u.ac.jp

January 30, 2001

Contents

1 INTRODUCTION

It is believed that elementary particles are quarks (and leptons) at present through the success of the quark model proposed by Gell-Mann [1] and Zweig [2]. However the quarks have never been measured as an isolated particle in nature, these exist with a color singlet combination of its color charge. This phenomenon is called the "Color Confinement". It is generally believed that the Quantum Choromodynamics (QCD) exhibits a phase transition at some temperature T_c, and quarks and gluons confined in the low temperature phase are liberated to form the "quark gluon plasma".

It seems that our universe was started from the Big Bang about twenty billion years ago with an extremely high temperature and density. Then the quark gluon plasma mentioned above is realized in the very early universe and go to the hadronic phase through the phase transition. (volume is increasing, T is decreasing) The study of QGP state and its phase transition are related with the various problems of the early universe. The QGP is one of the most energetic topics in the modern hadron physics.

Except for the early universe the QGP state may be created in a core of neutron star and high energy heavy ion collision experiments, however the only latter case has a possibility for its measurement in a laboratory. The search for the QGP state from the high energy heavy ion collision experiments had been examined since the end of the 1980's at CERN (European Laboratory for Particle Physics) and BNL (Brookhaven National Laboratory).

For these experiments the several signals of the QGP formation are considered, for example Strangeness and antibaryon enhancement [3, 4, 5, 6], 'exotic' signatures of the QGP [7], Photons and di-leptons pairs [8, 9], J/ψ suppression [10, 11] and Mass shift [10]. Many phenomena in the heavy ion collision experiment are consistent with the above signals and suggest a formation of QGP.

At the beginning of 2000, CERN reported that the QGP state had been created in the heavy ion collision experiment[23]. In these experiments, the J/ψ suppression[11] is regarded as the key signal of QGP formation. Since c-quark is heavy ($m_c = 1.15 \sim 1.35$ GeV[24]) $c\bar{c}$ pair are hard to be generated except by the primary collisions of nucleons in the high energy heavy ion, i.e. the J/ψ is not created with the thermal effects after the QGP formation. Therefor it is expected that the effects of deconfining clearly appear in this signal. Further investigation will be performed in RHIC project at BNL.

On the theoretical side, in spite of the various approaches[25, 26, 27], we are still far from the definite understanding of hadron properties near the transition and the fate of the hadronic states in the plasma phase. Since the phase transition changes the relevant degree of freedom of the system, the model approach which a priori assumes dynamical degrees of the system is difficult to treat physics near the phase transition.

I investigate these problems using lattice QCD, which enables us to incorporate the nonperturbative effect of QCD from the first principle.

The finite temperature field can be treated as the statistical ensemble, it is convenient with the lattice QCD formulation. However lattice QCD has serious problems for the finite density (chemical potential) systems [12]. In this case the fermion determinant becomes complex for non-zero values of the chemical potential μ and thus prohibits the use of conventional numerical algorithms. This problem has never been solved at the practical level. Thus the study of QGP with lattice QCD is almost restricted in the finite temperature system.

Since the finite temperature phase transition is confirmed by the lattice QCD, the determination of the critical temperature and the order of the phase transition have been investigated [13].

From the recent study the $T_c =\sim 270MeV$ and the 1st order phase transition are reported at the $N_f = 0$ (quenched simulation) [14, 15],where N_f is number of flavor.

With the dynamical quark effects in the case of $N_f = 2$, the lattice QCD predicts the $T_c =\sim 170MeV$ and the 2nd order phase transition with the Wilson fermion [16], on the other hand the $T_c =\sim 170MeV$ and the cross over with the Staggered fermion [17]. These inconsistent results of the Wilson fermion and the Staggered fermion are one of the open question of the lattice QCD. In the case of $N_f = 2 + 1$ (u,d and s quarks) close to the real world, status is still a level of research and development. [18]

With the lattice QCD it is possible to calculate the thermodynamical quantities of QGP from the partition function of QCD, e.g. energy density and pressure [15, 16, 19].

For a long time hadron masses at finite temperature have been argued with the spatial correlation which behaves an exponential decay with the screening mass [28]. This quantity reflects manifestations of some symmetries in the finite temperature system, e.g. chiral symmetry.

It is possible to discuss a fundamental degree of freedom in the QGP phase from the spatial correlators. Some works report that the hadronic plasma mode dominate just above T_c [20, 21], however other work claims these behaviors are consistent with a free quark gas picture at $T > 1.2T_c$ [22]. The spatial correlators give some suggestion for the nature of QGP.

On the other hand, the study of the temporal correlation, which is related to the pole mass, has been started rather recently[29].

The previous work[29] studied properties of hadrons composed of light quarks near T_c. They caught a sign of chiral symmetry restoration above T_c, and a change of correlators in temporal and spatial direction near the T_c. From the discussion of wave function, however, they find the same strong spatial correlation at $T > T_c$ as that of below T_c, in other words hadronic mode at a long range survives in the deconfinement

phase. At present, there is no well-established way of lattice simulations to attack the spectroscopy at $T > 0$. However, our recent work seems one of the best approaches to the problem. It is interesting to apply this analysis to the heavy quarks. In this paper I focus on the heavy quarkonium state, which plays an important role as a signal of the quark gluon plasma formation[11, 10].

Our goal of the investigation is the prediction about J/ψ suppression or mass shift of charmonium[10] as signals of QGP formation and the understanding of hadron properties and nature of QGP phase near the transition.

For the study of charmonium physics at $T > 0$ on a lattice, there are several problems. Then I classify these problems into two category, and discuss them individually.

(i) Precise calculation of temporal correlator of charmonium at $T > 0$

(ii) Extraction of physical properties of charmonium from the correlators

Firstly I consider the former one. In the lattice QCD simulation at $T > 0$, I set a temporal lattice extent to $1/T$. At high temperature, one needs the large lattice cutoff to work with the sufficient degrees of freedom in the temporal direction. In order to obtain the detailed information of temporal meson correlators at $T > 0$, a high resolution in temporal direction is needed. The large lattice cutoff is also necessary to study a correlator of meson with the heavy quarks because of its rapid decreasing behavior. If one tries to overcome these difficulties with straightforward way, the tremendous large computational power is necessary. In order to get the sufficiently fine resolution with limited computer resources, I use the anisotropic lattice, which has a finer temporal lattice spacing a_τ than the spatial one a_σ.

In this work I adopt the same strategy as the previous work[29] which was tractable to analyze light hadrons at $T > 0$. This strategy is as follows. Firstly the mesonic operator are defined, then I observe its correlator and wave function (in the Coulomb gauge) at $T = 0$. Next I investigate how they are affected by the temperature. In order to investigate the temperature effects for the state of interest, for example a ground and excited state of charmonium, I have to make the good mesonic operator which has the large overlap with the state. Because I should compare correlators at $T \geq 0$ within shorter temporal lattice extent. The wave function gives hints for existence of mesonic state at $T > 0$. Especially I am interested in that of deconfinement phase. In the case of charmonium this wave function is an important quantity concerning the J/ψ suppression.

I prepare two sets of gauge configuration whose lattice spacing are different. I control the temperature by changing temporal lattice extent N_t. Then above investigation is performed on these configurations.

This paper is organized as follows. In the next section I define the quark action on anisotropic lattice and discuss the dispersion relation of free quark and calibration of quark field. Sect. 3 is the preparation for study of charmonium correlator. Here various parameters of gauge configurations are determined and the calibration are performed. In Sect. 4 I report the charmonium spectroscopy and construction of optimized operator using variational analysis at $T = 0$. Sect. 5 describes correlators at $T > 0$ and the measurement of the wave function and compare these with results at $T = 0$. The last section is the conclusion and discussion.

2 Quark action on the anisotropic lattice

2.1 $O(a)$ improved Wilson quark formulation

The $O(a)$ improved version of Wilson fermionic action [31] (clover action) is widely used in current lattice simulations. Though it is straightforward generalization of that on isotropic lattice, anisotropy brings new ambiguity in addition to the choice of the clover coefficient of isotropic action.

In the following, firstly the isotropic $O(a)$ improved quark action is summarized as an introduction. Then the anisotropic version are described in the next subsubsection.

2.1.1 On the isotropic lattice

Dirac fermion Lagrangian in the continuum Euclidean space is

$$\mathcal{L} = \bar{\psi}_c(\gamma_\mu D_\mu + m_c)\psi_c \tag{1}$$

where γ_μ's are 4×4 hermitian matrices satisfying the relation $\{\gamma_\mu, \gamma_\nu\} = 2\delta_{\mu\nu}$. The physics is unchanged by the rescaling of the field. Since the fields ψ and $\bar{\psi}$ are treated as independent variables, they can be changed independently.

Let us consider the isotropic lattice first. (1) can be regarded as the lattice action enough close to the continuum limit. I apply following change of the fields:

$$\begin{aligned} \psi_c &= \left[1 - \frac{ra}{4}(\gamma_\mu D_\mu - m_c)\right]\psi, \\ \bar{\psi}_c &= \bar{\psi}\left[1 - \frac{ra}{4}(\gamma_\mu D_\mu - m_c)\right], \end{aligned} \tag{2}$$

where, r is a constant called as the Wilson parameter, and a is the lattice spacing. (One can use more general parameterization, but above changes are sufficient to derive common form of the clover action.) With these changes, the Lagrangian (1) changes as

$$\begin{aligned} \mathcal{L} &= \bar{\psi}\left[\gamma_\mu D_\mu + m_c + \frac{ra}{2}m_c^2 - \frac{ra}{2}\gamma_\mu D_\mu^2 + O(a^2)\right]\psi \\ &= \bar{\psi}\left[\gamma_\mu D_\mu + m - \frac{ra}{2}\left(D^2 + \frac{1}{2}g\sigma_{\mu\nu}F_{\mu\nu}\right) + O(a^2)\right]\psi. \end{aligned} \tag{3}$$

Here I put $m = m_c(1 + \frac{ra}{2}m_c)$ and used the definition [1]

$$\sigma_{\mu\nu} = -\frac{i}{2}[\gamma_\mu, \gamma_\nu], \tag{4}$$

$$gF_{\mu\nu} = i\,[D_\mu, D_\nu]. \tag{5}$$

With the discretization which is correct up to $O(a^2)$, this action has the same physical contents as the continuum action up to this order. The term with the coefficient r is

[1] These conventions are different from ones in the original paper [31].

a redundant operator. This term does not change the physics and is used to eliminate undesired fermion doubler with appropriate value of the Wilson parameter r. Except the term $\frac{ra}{4} g\sigma_{\mu\nu}F_{\mu\nu}$, the action (3) is same as the Wilson fermion action. This additional term is called as the clover term. (the name 'clover' comes from the clover-leaf definition of $F_{\mu\nu}$.)

Standard discretization of the derivatives are

$$D_\mu \rightarrow \frac{1}{2a_\mu}(T_{+\mu} - T_{-\mu}), \tag{6}$$

$$D_\mu^2 \rightarrow \frac{1}{a_\mu^2}(T_{+\mu} + T_{-\mu} - 2), \tag{7}$$

where $T_{+\mu}\psi(x) = U_\mu(x)\psi(x+\hat{\mu})$ and $T_{-\mu}\psi(x) = U_\mu^\dagger(x-\hat{\mu})\psi(x-\hat{\mu})$. The field strength $F_{\mu\nu}$ is expressed as

$$gF_{\mu\nu}(x) = -\frac{1}{4a_\mu a_\nu}\sum_{(x,\mu\nu)} \mathcal{I}[U_{(x,\mu\nu)}], \tag{8}$$

where $(x, \mu\nu)$ specifies four plaquettes open at x in $\mu - \nu$ plane. The operator $\mathcal{I}$ makes a matrix hermitian and traceless:

$$\mathcal{I}[M] \equiv \frac{M - M^\dagger}{2i} - \frac{1}{3}\mathrm{Im}(\mathrm{Tr}M). \tag{9}$$

Above definition of the $F_{\mu\nu}$ extract the linear term in F from the plaquette $U_{\mu\nu} \sim \exp(-igF_{\mu\nu})$.

Up to now, the treatment is restricted to the tree level. With quantum effect, the ratio of the term D^2 and clover term in the redundant term may change. This effect is expressed as a new parameter c_{SW}, the coefficient of the clover term.

For numerical simulation, it is more useful to introduce the the hopping parameter $\kappa = 1/2(m + 4r)$ and rescale the fermion field by the factor $\sqrt{2\kappa}$. With a common choice $r = 1$ and putting $a_\mu = a = 1$, the action reads

$$S = \sum_{x,y} \bar{q}(x)K(x,y)q(y), \tag{10}$$

$$\begin{aligned} K(x,y) &= \delta_{\mu\nu} - \kappa\sum_\mu \left[(1-\gamma_\mu)U_\mu(x)\delta_{x+\hat{\mu},y} + (1+\gamma_\mu)U_\mu^\dagger(x-\hat{\mu})\delta_{x-\hat{\mu},y}\right] \\ &\quad -\frac{\kappa r}{2}c_{\mathrm{SW}}g\sigma_{\mu\nu}F_{\mu\nu}, \end{aligned} \tag{11}$$

This action is referred as the 'Clover action' or '$O(a)$ improved Wilson action'.

To keep the $O(a)$ effect sufficiently small, careful choice of the clover coefficient c_{SW} is essential.

2.1.2 On the anisotropic lattice

Now I consider the $O(a)$ improved Wilson action on the anisotropic lattice. In this case the action has not necessarily take the symmetric form in space and time. I can choose the field rescaling as follows:

$$\begin{aligned}\psi_c &= \left[1-\frac{ra}{4}(\gamma_\mu D_\mu - m_c) - \frac{r'a}{4}\vec{\gamma}\cdot\vec{D}\right]\psi, \\ \bar{\psi}_c &= \bar{\psi}\left[1-\frac{ra}{4}(\gamma_\mu D_\mu - m_c) - \frac{r''a}{4}\vec{\gamma}\cdot\vec{D}\right].\end{aligned} \tag{12}$$

Here I introduce different parameters r' and r'' for fermion field and its conjugate. Though this is not a most general form, the nice feature of isotropic clover action is kept at most. As a, I can take the spatial lattice spacing. These changes leads

$$\begin{aligned}\bar{\psi}_c\{\gamma_\mu D_\mu + m_c\}\psi_c &= \bar{\psi}\Big\{(\gamma_\mu D_\mu + m_c) - \frac{r}{2}a[(\gamma_\mu D_\mu)^2 - m_c^2] \\ &\quad -\frac{(r'+r'')a}{4}\left[(\vec{\gamma}\cdot\vec{D})^2 + m_c\vec{\gamma}\cdot\vec{D}\right] \\ &\quad -\frac{a}{4}(r'\vec{\gamma}\cdot\vec{D}\gamma_4 D_4 + r''\gamma_4 D_4\vec{\gamma}\cdot\vec{D})\Big\}\psi.\end{aligned} \tag{13}$$

Observing the third line, it is useful to take $r' = r''$. Using the relations

$$\begin{aligned}(\vec{\gamma}\cdot\vec{D})^2 &= \vec{D}^2 + \frac{1}{2}g\sigma_{ij}F_{ij} \\ \{\vec{\gamma}\cdot\vec{D}, \gamma_4 D_4\} &= g\sigma_{i4}F_{i4},\end{aligned} \tag{14}$$

I reach to the form

$$\begin{aligned}\mathcal{L} &= \bar{\psi}\Big\{\gamma_\mu D_\mu + m - \frac{r}{2}a\left(D^2 + \frac{1}{2}g\sigma_{\mu\nu}F_{\mu\nu}\right) \\ &\quad -\frac{r'a}{2}\left[\vec{D}^2 + \frac{1}{2}g\sigma_{ij}F_{ij} + m_c\vec{\gamma}\cdot\vec{D}\right] - \frac{r'a}{4}g\sigma_{i4}F_{i4}\Big\}\psi.\end{aligned} \tag{15}$$

This expression is rather complicated to manage in general manner.

I therefore choose $r' = 0$. Namely I start with the action (3) and merely discretize it with different lattice spacings for space and time. Now taking $a_i = a$ and $a_4 = a/\xi$, where ξ is the anisotropy, and putting a unity, eq. (3) is written as

$$\begin{aligned}\mathcal{L} &= \bar{\psi}\frac{1}{\xi}\Big[m + \vec{\gamma}\cdot\vec{D} - \frac{r}{2}(\vec{D}^2 + \frac{1}{2}g\sigma_{ij}F_{ij}) \\ &\quad +\xi\gamma_4 D_4 - \frac{r}{2}(\xi^2 D_4^2 + \xi g\sigma_{i4}F_{i4})\Big]\psi.\end{aligned} \tag{16}$$

The bare quark mass m is in the unit of the spatial lattice spacing.

For later convenience, I replace r with ξ^{-1} only at the term with D_4^2, and at other place leave it as r.

$$\begin{aligned} S &= \sum_{x,y}\bar{\psi}(x)\Bigg[\frac{m+\xi+3r}{\xi} - \frac{1}{2}\Big\{(1-\gamma_4)U_4(x)\delta_{x+\hat{4},y} + (1+\gamma_4)U_4^\dagger(x-\hat{4})\delta_{x-\hat{4},y}\Big\} \\ &\quad -\frac{1}{2\xi}\sum_i\Big\{(r-\gamma_i)U_i(x)\delta_{x+\hat{i},y} + (r+\gamma_i)U_i^\dagger(x-\hat{i})\delta_{x-\hat{i},y}\Big\} \\ &\quad -\frac{r}{2}c_E\sigma_{4i}F_{4i}(x)\delta_{x,y} - \frac{r}{4\xi}c_B\sigma_{ij}F_{ij}(x)\delta_{x,y}\Bigg]\psi(y). \end{aligned} \tag{17}$$

Here I introduced the clover coefficients c_E and c_B, which are unity at the tree level.

Now let us transform above action into the hopping parameter form. I define

$$\kappa_s = \frac{1}{2(m+\xi+3r)}, \tag{18}$$

$$\kappa_t = \xi\kappa_s. \tag{19}$$

Rescaling $\psi \to \sqrt{2\kappa_t}\psi$,

$$S = \sum_{x,y}\bar{\psi}(x)K(x,y)\psi(y), \tag{20}$$

$$\begin{aligned} K(x,y) &= \delta_{x,y} - \kappa_t\Big\{(1-\gamma_4)U_4(x)\delta_{x+\hat{4},y} + (1+\gamma_4)U_4^\dagger(x-\hat{4})\delta_{x-\hat{4},y}\Big\} \\ &\quad -\kappa_s\sum_i\Big\{(r-\gamma_i)U_i(x)\delta_{x+\hat{i},y} + (r+\gamma_i)U_i^\dagger(x-\hat{i})\delta_{x-\hat{i},y}\Big\} \\ &\quad -r\kappa_t c_E g\sigma_{4i}F_{4i}(x)\delta_{x,y} - r\kappa_s c_B\frac{1}{2}g\sigma_{ij}F_{ij}(x)\delta_{x,y}. \end{aligned} \tag{21}$$

This is one of the form of the $O(a)$ improved Wilson quark action on the anisotropic lattice. There are several ways to define such an action on anisotropic lattice. The action defined by P. Chen [33] is constructed using an anisotropy for the rescaling of the field. On the other hand our action are kept as the isotropic form. These details are mentioned in the next section.

2.2 Quark action for the charm quark

To treat the quark field on the lattice, I adopt the $O(a)$ improved Wilson quark formulation. To construct the quark action on the anisotropic lattice, I follow El-Khadra, Kronfeld and Mackenzie[30], for the following advantages. They expand the lattice Hamiltonian in the power of a, and determine the coefficient of each operator by matching the lattice Hamiltonian with the the continuum one except the redundant operators. The resultant action takes the same form as the clover quark action[31] in the limit of $m \to 0$. On the other hand, in the heavy quark mass region ($m_q \gg \Lambda_{QCD}$), the effective-theoretical treatment of the quark action enables us to use it for such a quark

on a lattice of moderate cutoff. Since the full quark mass dependence is incorporated, the same form also covers the intermediate quark mass region, and then the small and the large mass regions are smoothly connected. Although our main target in this paper is the charm quark, it would be useful to take the other mass region into account for the future applications. In addition to these advantages, their argument is naturally in accord with the anisotropic lattice. They introduced the different hopping parameters for the spatial and the temporal directions, and proposed to tune them so that the rest and the kinetic mass take the same value. Such a treatment is inevitably required on the anisotropic lattice to assure that the anisotropy of the quark and the gauge fields coincide, especially if one employ the dispersion relation for the definition of the quark field anisotropy.

On the anisotropic lattice, the quark action takes almost the same form as in the Ref. [30] [2] :

$$S_F = \sum_{x,y} \bar{\psi}(x) K(x,y) \psi(y), \tag{22}$$

$$\begin{aligned} K(x,y) &= \delta_{x,y} - \kappa_\tau \left\{ (1-\gamma_4) U_4(x) \delta_{x+\hat{4},y} + (1+\gamma_4) U_4^\dagger(x-\hat{4}) \delta_{x-\hat{4},y} \right\} \\ &\quad - \kappa_\sigma \sum_i \left\{ (r-\gamma_i) U_i(x) \delta_{x+\hat{i},y} + (r+\gamma_i) U_i^\dagger(x-\hat{i}) \delta_{x-\hat{i},y} \right\} \\ &\quad - \kappa_\sigma c_E \sum i \sigma_{4i} F_{4i}(x) \delta_{x,y} - r \kappa_\sigma c_B \sum_{ij} \frac{1}{2} \sigma_{ij} F_{ij}(x) \delta_{x,y}. \end{aligned} \tag{23}$$

The spatial and the temporal hopping parameters, κ_σ and κ_τ respectively, are related to the bare quark mass m_0 and the bare anisotropy parameter γ_F as follows.

$$\kappa_\sigma = \frac{1}{2(m_0 + \gamma_F + 3r)}, \tag{24}$$

$$\kappa_\tau = \gamma_F \kappa_\sigma. \tag{25}$$

where the m_0 is in the spatial lattice unit. In the free quark case, the bare anisotropy γ_F is taken to be the same value as the cutoff anisotropy $\xi = a_\sigma / a_\tau$. In practical simulation, the anisotropy parameter receives the quantum effect and should be tuned to give the same renormalized anisotropy for the fermion and the gauge fields. This "calibration" will be described later.

There have been used two choices of the value of the Wilson parameter r for the anisotropic $O(a)$ improved quark action. In this work, I adopt the choice[29] $r = 1/\xi$. In this case, the temporal and the spatial directions are treated in the equal manner in the physical unit. As the result, the tree level dispersion relation holds the axis-interchange symmetry in the lowest order of $\vec{p}^2$. On the other hand, this choice decreases the masses

[2] The notation in this paper is slightly different from the Ref. [30] .

of doublers which are introduced by the Wilson term to eliminate the unwanted poles at the edges of the Brillouin zone. The dispersion relation is examined in the later part of this section. Alternative choice, $r = 1$, are adopted in the Ref. [32, 33, 34]. In this case, the contribution of doublers would not cause any problem, in the cost of manifest axis-interchange symmetry. Since I aim to develop the form applicable to the whole quark mass region, $r = 1/\xi^{-1}$ seems preferable especially in the light quark mass region.

Here it is useful to define κ so that which has the same relation with the bare quark mass m_0 as the isotropic case:

$$\frac{1}{\kappa} = \frac{1}{\kappa_\sigma} - 2(\gamma_F + 3r - 4) \quad (= 2(m_0 + 4)\,). \tag{26}$$

For the light quark systems, the extrapolation to the chiral limit would be performed in $1/\kappa$. The coefficients of the clover terms, c_E and c_B, depend on the Wilson parameter r. In our choice $r = \xi^{-1}$, c_E and c_B are unity at the tree level.

I apply the mean-field improvement proposed in the Ref. [35]. On the anisotropic lattice, the mean-filed values of the spatial link variable u_σ and the temporal one u_τ are different from each other. The improvement is achieved by rescaling the link variable as $U_i(x) \to U_i(x)/u_\sigma$ and $U_4(x) \to U_4(x)/u_\tau$. This replacement leads the following values for the coefficient of the clover terms.

$$c_E = \frac{1}{u_\sigma u_\tau^2}, \quad c_B = \frac{1}{u_\sigma^3}. \tag{27}$$

The determination of mean-field values of the link variable u_σ and u_τ are described in the next section.

In this paper, our target mass region is around the charm quark mass. The temporal cutoffs in this work are 4.5 and 6.4 GeV, and well above the charm quark mass. For these quark mass and a_τ^{-1}, the effective-theoretical treatment would not be necessary to be applied. Such consideration will be called for the calculations containing the b-quark on the same size of lattice. In the effective-theoretical treatment, the ratio of the spatial and the temporal hopping parameter is tuned so that they give correct dispersion relation of the nonrelativistic quark[30]. On the anisotropic lattice, the calibration automatically incorporates this condition if one use the nonrelativistic dispersion relation as the anisotropy condition.

2.3 Dispersion relation of free quark

Now I consider how the dispersion relation of the free quark is changed by the introduction of anisotropy. Observing the action (23), one notices that the larger anisotropy ξ causes the smaller spatial Wilson term. Then the question is how the contribution of

the doubler eliminated by the Wilson term becomes significant. The action (23) leads the free quark propagator,

$$S(p) = \frac{1}{i\gamma_4 \sin p_4 + i\,\zeta\vec{\gamma}\cdot\vec{S} + m_t + (1-\cos p_4) + \frac{1}{2}r\zeta\vec{\hat{p}}^2}, \tag{28}$$

where $\zeta = \xi^{-1}$, $m_t = m_0\zeta$, $S_i = \sin p_i$ and $\hat{p}_i = 2\sin(p_i/2)$. The correlator $C(\vec{p},t)$ for $t > 0$ is

$$\begin{aligned} C(\vec{p},t) &= \int_{-\pi}^{\pi}\frac{dp_4}{2\pi}S(p)e^{ip_4 t} \\ &= \frac{e^{-E(\vec{p})t}}{u(\vec{p})}\frac{1}{2\sinh E(\vec{p})}\{\gamma_4\sinh E(\vec{p}) - i\zeta\vec{\gamma}\cdot\vec{S} + u(\vec{p}) + \cosh E(\vec{p})\} \end{aligned} \tag{29}$$

where $u(\vec{p}) = m_t + 1 + r\zeta\vec{\hat{p}}^2/2$.

Then the dispersion relation of the free quark is

$$\cosh E(\vec{p}) = 1 + \frac{\zeta^2\vec{S}^2 + (m_t + \frac{1}{2}r\zeta\vec{\hat{p}}^2)^2}{2(1 + m_t + \frac{1}{2}r\zeta\vec{\hat{p}}^2)}. \tag{30}$$

Neglecting the higher order terms in $\vec{p}$ and in a, the relativistic dispersion relation $E^2 = m^2 + \zeta^2\vec{p}^2$ holds for the small quark mass. ($m^2 = m_t^2(1-m_t)$, and m_t is the bare parameter.)

Fig. 1 shows the dispersion relation (30) at $\xi = 5.3$ and 4.0 for various values of m_t. Now let us consider the practical cases that $a_\tau^{-1} = 4.5$ GeV for $\xi = 5.3$ (Set-I) and $a_\tau^{-1} = 6.4$ GeV for $\xi = 4.0$ (Set-II). These values are obtained in our numerical simulations, and described in the next section. In the heavy quarkonium, the typical energy and momentum exchanged inside the meson are in the order of mv^2 and mv respectively[36]. For the charmonium, $v^2 \sim 0.3$, then typical scale of the kinetic energy is around 500 MeV. It is noted that $m_t \sim 0.3$ for Set-I and $m_t \sim 0.2$ for Set-II correspond to the charm quark mass. Let us consider two quarks inside meson with opposite momenta $p = \pm\pi/a$. Then $2(E(p_z = a/\pi) - E(0)) \sim 0.5$ GeV and ~ 1 GeV for Set-I and Set-II respectively. Although Set-I lattice may not be free from the systematic effect, Set-II would be successfully applicable to the low-lying charmonium system.

For comparison, I also examine the light quark mass region. For Set-I, $m = 0.02$–0.06 corresponds to 90-270 MeV, which is used in the Ref. [29] as the light quark mass region with the anisotropic Wilson quark action with $r = 1$. $E(\vec{p}) - E(0)$ rapidly decrease at the edge of the Brillouin zone, and the height at $z = a/\pi$ is around 300 MeV. For two quarks with momenta $p = \pm a/\pi$, additional energy of doublers is ~ 600 MeV, and again seems not sufficiently large compared with the typical energy scale transfered inside mesons. In the case of Set-II, this value increases to 1.4 GeV, and seems to be applicable to the meson systems without large systematic effect.

2.4 Calibration of quark field

On anisotropic lattice, the anisotropy of quark configuration ξ_F must be equal to that of gauge field ξ.

$$\xi(\gamma_G, \gamma_F) = \xi_F(\gamma_G, \gamma_F) \tag{31}$$

Since ξ and ξ_F are function of γ_G and γ_F in general, a nonperturbative determination of the combination of γ_G and γ_F which satisfy the condition (31) requires much effort. In the quenched case, however, these determination are rather easy to be performed, because ξ can be determined independently of γ_F. After the determination of ξ, one can tune γ_F so that the certain observable satisfies the condition (31). I call this procedure as "calibration".

There are several determinations of ξ_F. In the Ref. [29], the ratio of the temporal to the spatial meson masses, $\xi_F = m_\sigma/m_\tau$, is used as such a observable. However this is not suitable for the present case, since the charm quark mass is larger than or comparable with the spatial lattice cutoffs. In order to determine ξ_F, I use the dispersion relation of the free meson[32, 33, 34]. For a heavy quark, one may use the nonrelativistic dispersion relation, $E = m + p^2/2m\xi_F^2$. In this paper, I alternatively use the relativistic dispersion relation of meson for the calibration. This form is also available for the light quark mass region.

I assume that the meson is described by the following lattice Klein-Gordon action.

$$S = \sum_x \frac{1}{2\xi_F}\phi^\dagger(x)\left[-\xi_F^2 D_4^2 - \vec{D}^2 + m_0^2\right]\phi(x), \tag{32}$$

where m_0 is in the unit of a_σ. Then the free meson satisfies the dispersion relation

$$\cosh E(\vec{p}) = 1 + \frac{1}{2\xi_F^2}(\vec{\hat{p}}^2 + m_0^2). \tag{33}$$

Using this relation, one can determine the anisotropy ξ_F as

$$\xi_F^2 = \frac{\vec{\hat{p}}^2}{2(\cosh E(\vec{p}) - \cosh E(0))} \tag{34}$$

This condition forces the axis-interchange symmetry to the meson field.

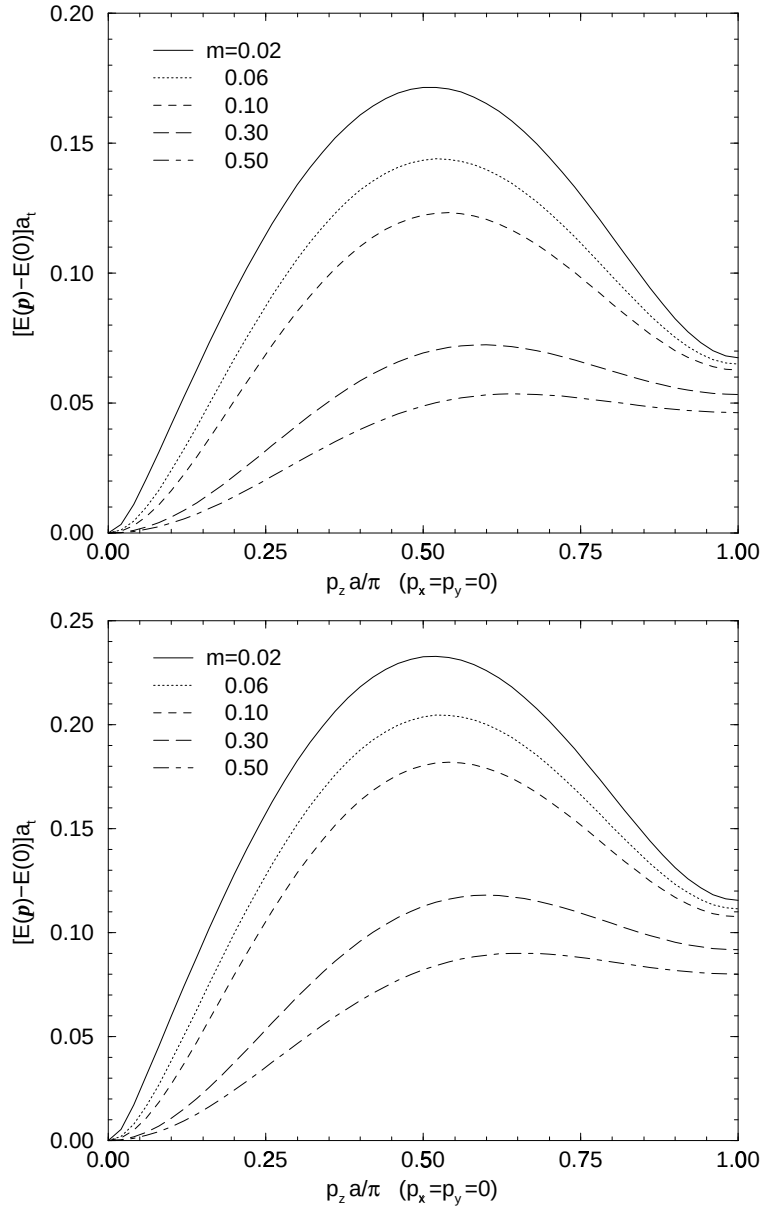

Figure 1: Dispersion relation of anisotropic free quark. Top figure is of Set-I, bottom one is of Set-II.

3 Lattice setup

3.1 Gauge configuration

The numerical calculations performed on the two sets of anisotropic lattices[37], one is with the standard plaquette action and the other is with Symanzik type improved action at the tree level[38]. These actions are represented with the following form;

$$\begin{aligned} S_G &= \frac{\beta}{\gamma_G}\sum_{x,i<j\leq 3}[c_{11}(1-P_{ij}(x))+c_{12}(2-R_{ij}(x)-R_{ji}(x))] \\ &\quad +\beta\gamma_G\sum_{x,i\leq 3}[c_{11}(1-P_{i4}(x))+c_{12}(2-R_{i4}(x)-R_{4i}(x))]\,, \end{aligned} \tag{35}$$

where the plaquette $P_{\mu\nu}(x)$ and rectangular loop $R_{\mu\nu}(x)$ are defined as follows,

$$P_{\mu\nu} \equiv \frac{1}{3}\mathrm{ReTr}[U_\mu(x)U_\nu(x+\hat{\mu})U_\mu^\dagger(x+\hat{\nu})U_\nu^\dagger(x)] \tag{36}$$

$$R_{\mu\nu} \equiv \frac{1}{3}\mathrm{ReTr}[U_\mu(x)U_\mu(x+\hat{\mu})U_\nu(x+2\hat{\mu})U_\mu^\dagger(x+\hat{\nu}+\hat{\mu})U_\mu^\dagger(x+\hat{\nu})U_\nu^\dagger(x)]. \tag{37}$$

The standard action is the case with $c_{11}=1$ and $c_{12}=0$, and the improved action is $c_{11}=5/3$ and $c_{12}=-1/12$. The Set-I is the same configurations as used in the Ref. [29]. The parameters for these configurations are summarized in Table 1. These parameters are adopted so that the spatial and temporal lattice extent are about 3 fm respectively.

Both numerical calculations are done on the quenched configurations which are generated by the pseudo-heat bath algorithm with 20,000 thermalization sweeps, the configurations being separated by 2,000 sweeps. These configurations are fixed to Coulomb gauge. The statistical errors are estimated using the jackknife method unless mentioned explicitly.

3.2 Determination of the lattice constants

I determine the parameters for the gauge field configurations, renormalized anisotropy $\xi(\equiv a_\sigma/a_\tau)$, spatial cutoff scale a_σ^{-1} and mean-field values. At $T>0$ I have to determine the critical temperature.

In this section I show the detailed analysis for Set-II.

Set	c_{11}	c_{12}	size	β	γ_G	# conf.
Set-I	1	0	$12^3\times N_t$	5.68	4.00	60
Set-II	5/3	-1/12	$16^2\times 24\times N_t$	4.56	3.45	120

Table 1: Simulation parameters for the gauge configurations.

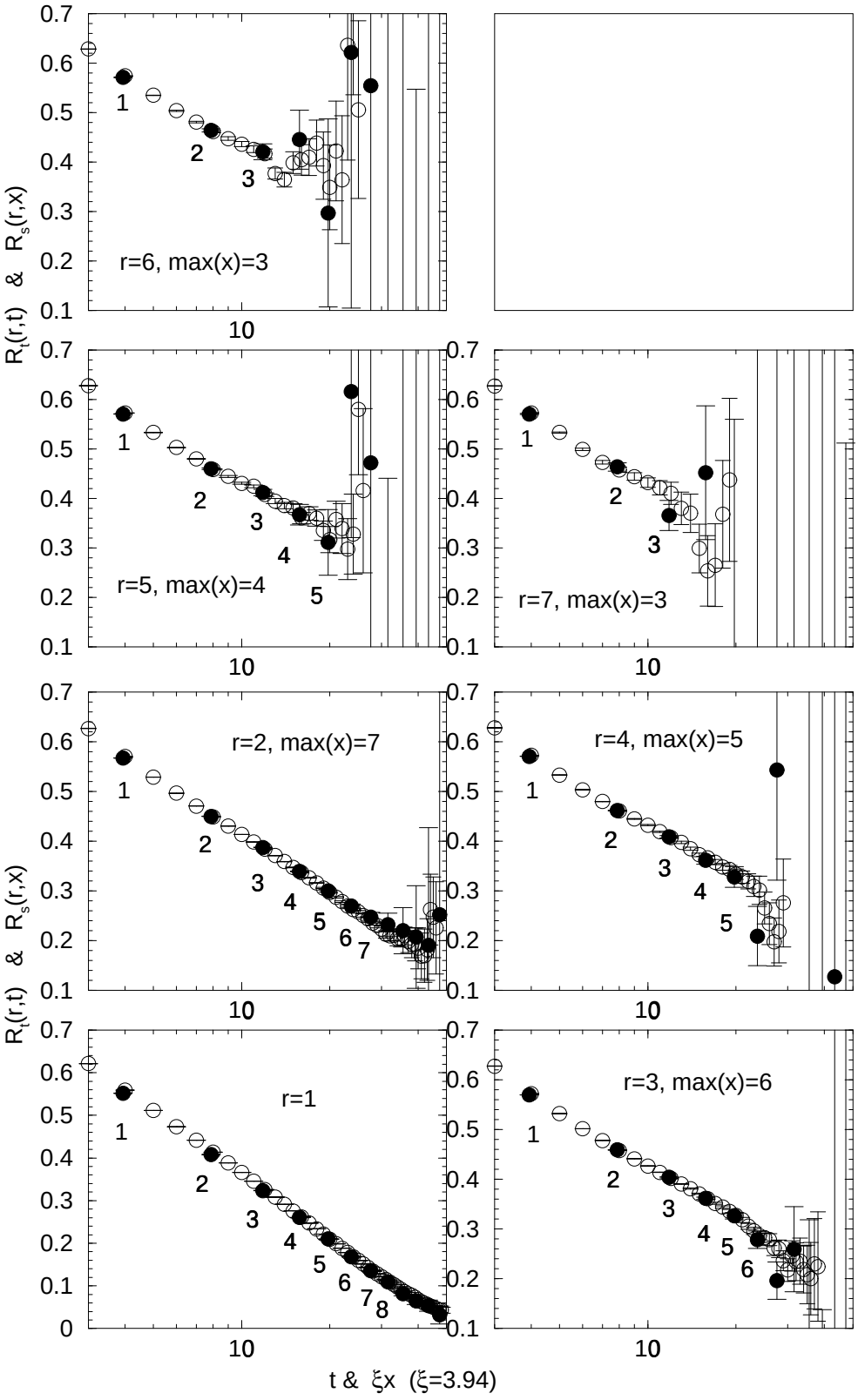

Figure 2: The ratio of Wilson loops, $R_\sigma(r,x)$ and $R_\tau(r,t)$.

3.2.1 Renormalized anisotropy

I define the ratios of the Wilson loop on spatial-spatial ($\sigma\sigma$) and spatial-temporal ($\sigma\tau$) plane[39, 40, 41].

$$R_\sigma(r,x) = W_{\sigma\sigma}(r,x)/W_{\sigma\sigma}(r+1,x), \quad (38)$$

$$R_\tau(r,t) = W_{\sigma\tau}(r,t)/W_{\sigma\tau}(r+1,t) \quad (39)$$

Then ξ is determined so that the matching condition, $R_\sigma(r,x) = R_\tau(r,t=\xi x)$, is satisfied. Figure 2 shows $R_\sigma(r,x)$ and $R_\tau(r,t)$ at each r, then $R_\sigma(r,x)$ are rescaled with $\xi = 3.95$ in these figures.

In practice I search for a minimization point of $L(\xi)$,

$$L(\xi) = \sum_{r,x} \frac{R_s(r,\xi x) - R_t(r,t)}{d(R_s)^2 + d(R_t)^2}, \quad (40)$$

where $d(R_s)$ and $d(R_t)$ are statistical error of R_s and R_t, and $R_s(r,t)$ in eq.(40) is interpolated with the cubic spline in respect of t. The range of summation over r and x is determined by the following policy.

- For removing cutoff effects, I exclude the data for $r = 1$ and $r \times x \leq \min(r \times x)$
- At each r the maximal x, max$x$, are determined by hand from Fig. 2

Figure 3 shows the $\min(r \times x)$ dependence of the renormalized anisotropy ξ. From the Fig. 3, xi gives a stable value at $r \times x \leq 8$, then I conclude $\xi = 3.950(18)$ for Set-II. I have $\xi = 5.3(1)$ with the same analysis for Set-I.

3.2.2 Cutoff scale

Cutoff scales are determined from the static quark potential using the physical value of the string tension. In order to calculate the static quark potential efficiently, I use the Bali and Schilling's smearing technique [48] with the coefficient of the staple summation $c = 2.30$. I prepare the smeared configurations up to 40 smearing steps every 2 steps. For each spatial distance "r", I adopt a number of smearing where the overlap function $C(r)$ is the nearest to unity, where the $C(r)$ is defined by the following ansatz.

$$W_{st}(r,t) = C(r)\exp\left(-V(r)t\right) \quad (41)$$

Then the static quark potential $V(r)$ is extracted from the fitting $W_{st}(r,t)$ on the smeared configuration to the Eq.(41).

Figure 4 shows the effective mass plots for each r.

In order to extract the string tension σ from the static quark potential $V(r)$, I use the following potential fitting ansatz,

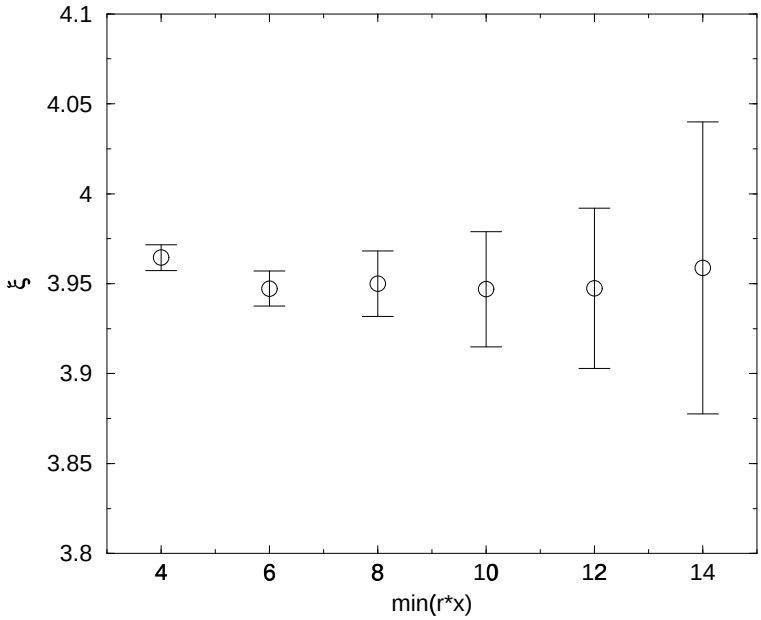

Figure 3: The $\min(r \times x)$ dependence of the renormalized anisotropy ξ.

$$V(r) = A + \frac{\alpha}{r} + \sigma r, \tag{42}$$

where I use the $V(r)$ data which has larger $C(r)$ than 0.80 (in practice up to $9a_s$).

In this analysis I try to fit with 3-parameters and 2-parameters, in the later case α is fixed to $-\pi/12\xi$. For each case I calculate with $R_{\rm min} = 1.0a_s \sim 4.0a_s$. The fitting results of the Coulomb term coefficient α and the string tension σ are shown in Fig. 5,6.

Then the fitting results are stable at $R_{\rm min} \geq 2.8a_s$. The static quark potential and 3-parameters fitting results are shown in Figure 7 and these relative deviation is in Figure 8, where the relative deviation is defined in Eq.43.

$$V_{\rm rela}(r) = \frac{V(r) - V_{\rm fit}(r)}{V_{\rm fit}(r)}. \tag{43}$$

Finally I summarize the results of the static quark potential in Table 2.

With $\sqrt{\sigma_{\rm phys}} = 427$MeV[42], the spatial cutoff scales are $a_\sigma^{-1} = 0.85(3)$ GeV (Set-I) and 1.610(14) GeV (Set-II) respectively.

3.2.3 Critical temperature

In order to determine the critical temperature, I calculate the Polyakov loop and its susceptibilities at $N_t = 22, 24, 25$ and 26 for Set-II.

Set	A	α	σ	χ^2/d.o.f
Set-I	0.104(16)	-0.041(24)	0.0480(23)	2.45
Set-II	0.1599(25)	-0.0587(49)	0.01781(29)	4.34

Table 2: The results of static quark potential. I do not show only for Set-II but also for Set-I.

N_t	Polyakov loop	susceptibility	bin size
22	0.0848(18)	0.000094(20)	3,000
24	0.0471(78)	0.00036(18)	6,000
25	0.0139(19)	0.000093(30)	2,000
26	0.0127(12)	0.0000575(94)	2,000

Table 3: The Polyakov loop and its susceptibility for Set-II.

These quantities are measured every 10 sweeps up to 40,000 sweeps (20,000 sweeps for $N_t = 22$), thermalization is 10,000 sweeps (5,000sweeps). Error is estimated by the jackknife method. The histories of rotated Polyakov loop are summarized in Fig.9.

For $N_t = 24$ and 25 I carry out the Histogram method [49], then I get the results of Fig.10.

From these analysis of Polyakov loops and its susceptibilities, I find that the temperature of lattices with $N_t = 18$ (Set-I) and 24 (Set-II) are both just above T_c. Then I estimate $T_c = 250 \sim 260$ MeV from the temporal cutoff scale on our lattices. These estimation are consistent with the other quenched lattice results. I prepare the finite temperature gauge configurations at just below T_c, just above T_c and about $1.5T_c$ for each sets. These results are summarized in Table 4.

Here I notice that the hadronic correlator depends on which the sector Polyakov loop stays in Z_3 space at $T > T_c$. Since I treat the quenched QCD as an approximation of the full QCD, I choose the real sector for the value of Polyakov loop at $T > T_c$.

Set	ξ	a_σ^{-1}(GeV)	a_τ^{-1}(GeV)	$N_t(T/T_c)$
Set-I	5.3(1)	0.85(3)	4.5(2)	72 ($\sim$ 0), 20 (0.93), 16 (1.15), 12 (1.5)
Set-II	3.950(18)	1.610(14)	6.359(62)	96 ($\sim$ 0), 26 (0.93), 22 (1.10), 16 (1.52)

Table 4: Scale parameters for the gauge configuration. The ξ_F, a_σ^{-1} and a_τ^{-1} are measured on the configurations at $T = 0$ ($N_t = 72$ (Set-I), 96 (Set-II)). Here the temperatures are roughly estimated in the unit of T_c.

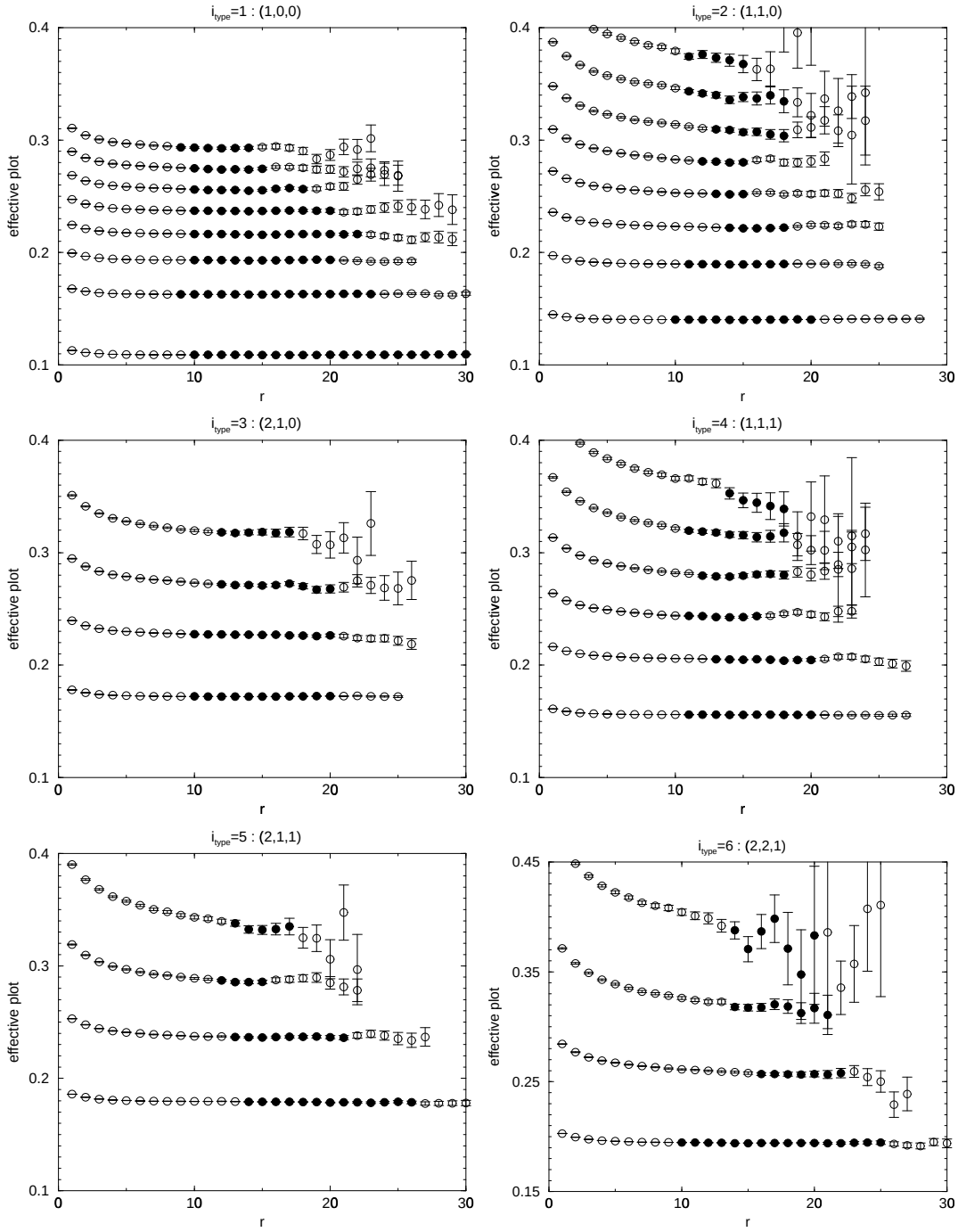

Figure 4: The effective mass plots of the Wilson loops.

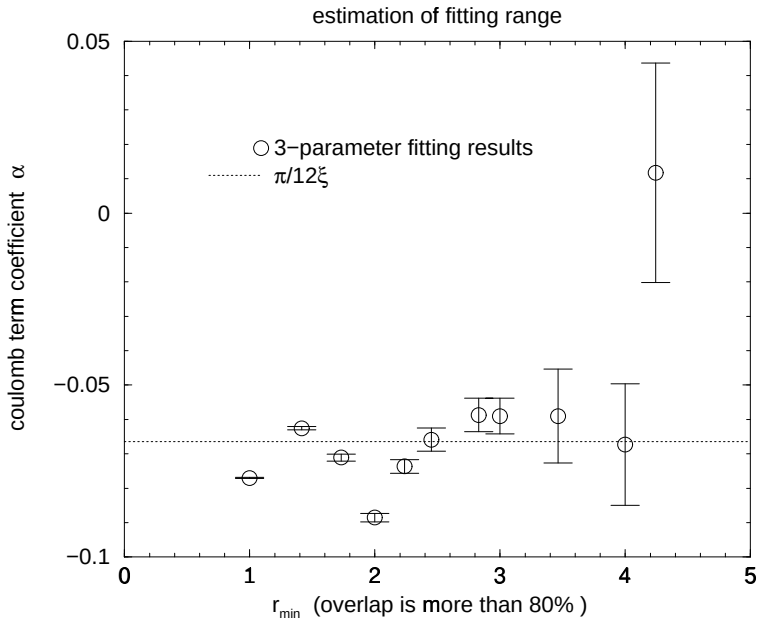

Figure 5: The fitting results of the Coulomb term coefficient.

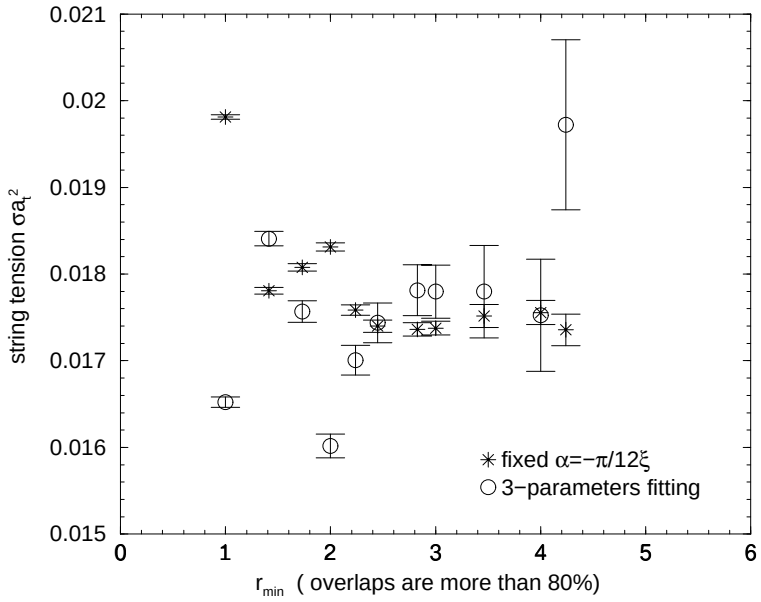

Figure 6: The fitting results of the string tension.

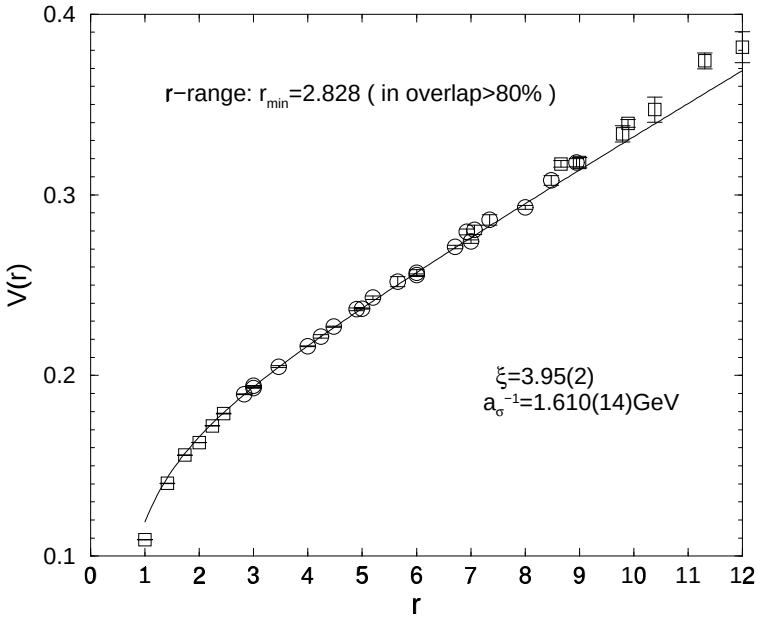

Figure 7: The result of static quark potential.

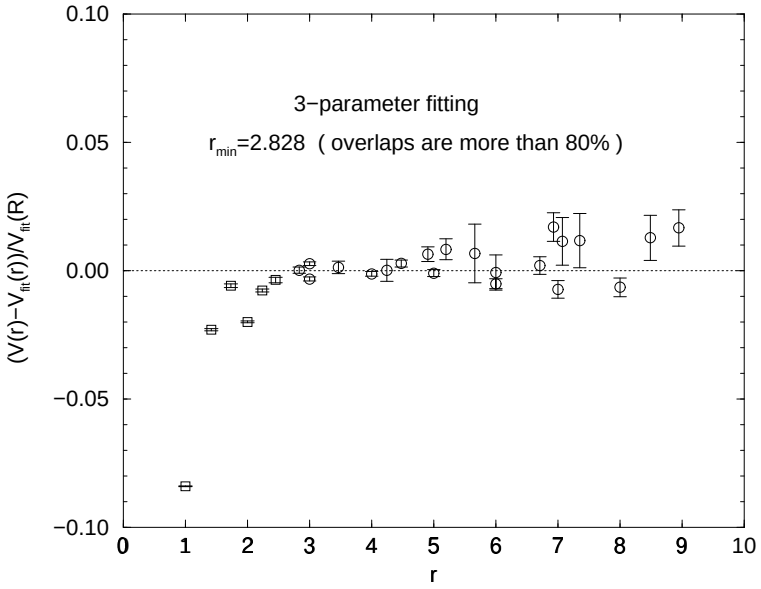

Figure 8: The relative deviation of the static quark potential.

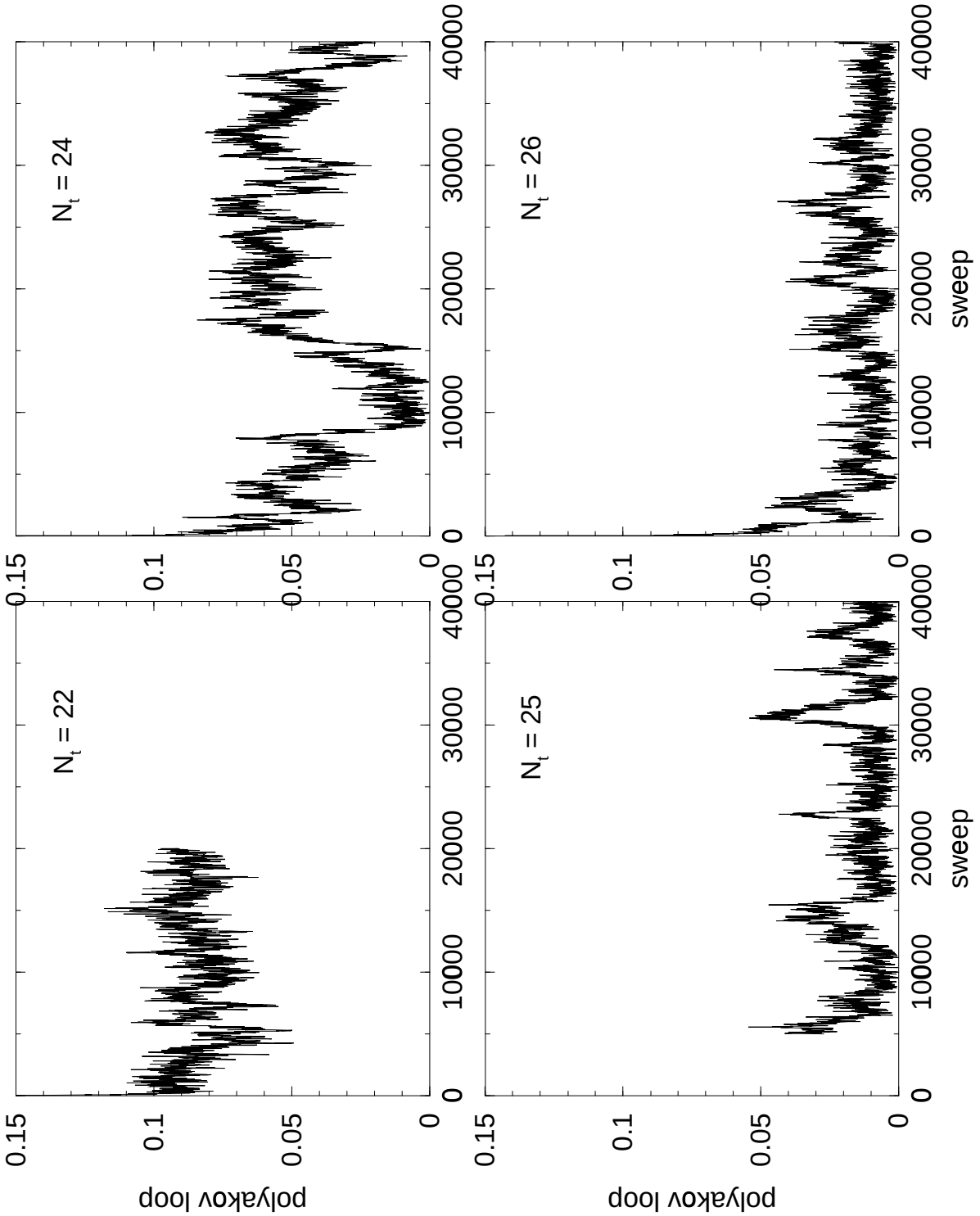

Figure 9: The history of the rotated Polyakov loop.

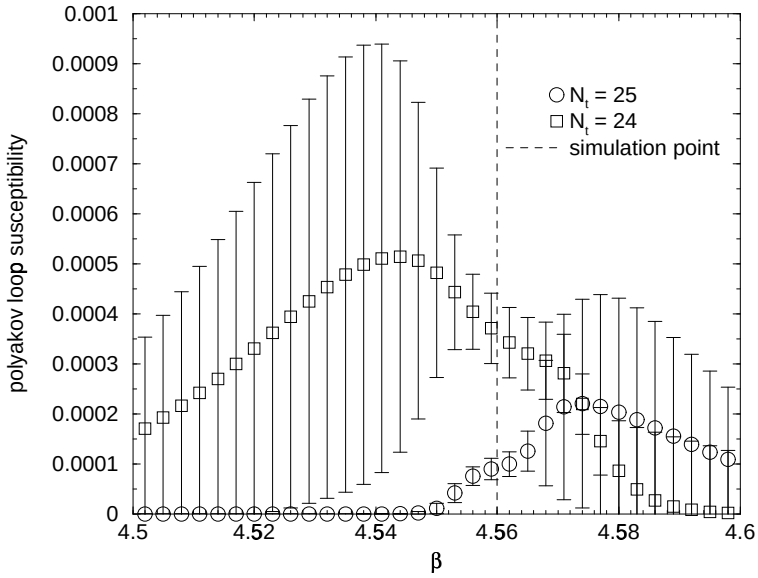

Figure 10: The results of the Histogram method for the Polyakov loop susceptibility.

3.2.4 Mean-field value on the anisotropic lattice

I state the calculation of mean-filed value on the anisotropic lattice for the mean-field improvement of the clover coefficients.

There are two commonly used methods. One is determined from the expectation value of plaquette. This is widely used for its easiness to measure. On anisotropic lattice these are determined as follows.

$$u_\sigma = \frac{1}{3}\langle \mathrm{ReTr} P_{ij}(x)\rangle^{\frac{1}{4}}, \quad u_\tau = \frac{1}{3u_\sigma}\langle \mathrm{ReTr} P_{i4}(x)\rangle^{\frac{1}{2}} \tag{44}$$

The other is the trace of link calculated in the Landau gauge.

$$u_\sigma = \frac{1}{3}\langle \mathrm{ReTr} U_i(x)\rangle, \quad u_\tau = \frac{1}{3}\langle \mathrm{ReTr} U_4(x)\rangle \tag{45}$$

In the former case u_τ is greater than the unity on our lattice. Then the latter definition seems more reasonable. In this work I determined the mean-field values in the Landau gauge.

The Landau gauge fixing is realized by maximization of Eq.(46).

$$\sum_x \mathrm{ReTr}\left(U_1(x) + U_2(x) + U_3(x) + c_{st}U_4(x)\right) \tag{46}$$

Here, the temporal coefficient c_{st} appears on the anisotropic lattice. I adopt the self-consistent mean-field improvement of c_{st}. As the tree level I chose $c_{st} = \xi^2$. Using the mean-field improved $c_{st} = \xi^2 u_\sigma/u_\tau$ I calculate the mean-field values recursively. I perform these calculation with 20 configurations. In our case, the result of 3rd measurement is consistent with the input u_σ/u_τ which is determined from the linear interpolation of the tree level and first mean-field improvement result. These results are summarized in Table 5 together with the mean-field improved c_E and c_B. Here I mention that the mean-field improved γ_G give the reasonable estimation for ξ within 1% (Set-I) and 6% (Set-II) error.

3.3 Calibration result

I now turn to the calibration of quark field. It is performed by the Eq.(33) with the momentum $\vec{p} = (0,0,0)$ and $(0,0,1)$ for each mesonic channel, pseudoscalar (Ps) and

Set	u_σ	u_τ	c_E	c_B
Set-I	0.75050(16)	0.992436(13)	1.7889	2.3656
Set-II	0.812354(92)	0.9900788(90)	1.5305	1.8654

Table 5: Mean-field value of link variable and mean-field improved clover coefficients for each sets.

vector (V). These results are summarized in Fig. 11. These calibrations are performed at the parameters which correspond to the pseudoscalar mass $m_{Ps} \simeq 2.6,\ 3.0$ and 3.4 GeV respectively.

The detailed definition of meson correlator which is adopted here is shown in Sect. 4.1 In these calculations I use the smeared source function which is determined from the wave function at $1/\kappa = 9.868$ (Set-I) and $\kappa = 8.797$ (Set-II). Here I mention that the shape of wave function has very weak κ dependence.

From the Fig. 11, I find that the γ_F dependence of ξ_F is almost linear and κ dependence of its slope is small. The γ_F which is determined from the pseudoscalar and the vector gives consistent value within the statistical error for each κ. Especially ξ_F for Set-II are in good agreement with the pseudoscalar and the vector. I determine the γ_F which satisfies the condition of Eq.(31) from the interpolation with the linear fitting. The error of γ_F is estimated from the error of ξ and ξ_F. These calibration results are summarized in Table 6. Here I mention that the mean-field improved γ_F give the reasonable estimation for ξ_F within 9% (Set-I) and 1% (Set-II) error.

	$1/\kappa$	κ_s	γ_F
	10.300	0.093545	3.629(91)
Set-I	9.868	0.096098	3.703(84)
	9.480	0.098599	3.765(79)
	9.041	0.110350	3.251(52)
Set-II	8.797	0.113121	3.262(49)
	8.590	0.115564	3.272(47)

Table 6: Calibration results for Set-I and Set-II. These parameters satisfy the condition of $\xi = \xi_F$ within the statistical error for the both mesonic channel. The error of γ_F is estimated from the error of ξ and ξ_F

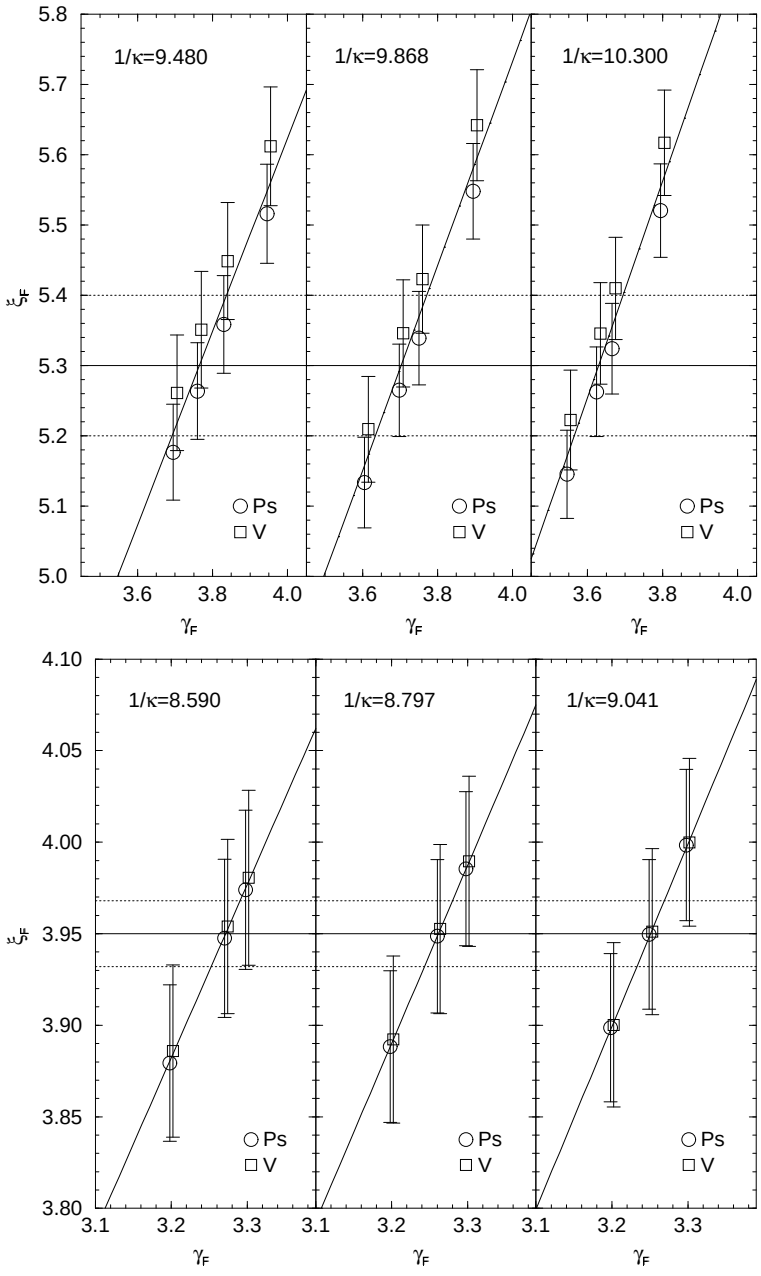

Figure 11: The top figure shows the calibration for Set-I and the bottom one is for Set-II. In the both figures, values of ξ (=5.3(1) (Set-I) and =3.950(18) (Set-II)) are indicated. The three values of κ correspond to a pseudoscalar mass $m_{\rm Ps} \simeq 2.6,\ 3.0$ and 3.4 GeV respectively.

4 Results at Zero temperature

4.1 Meson correlators

The mesonic operator which is used in this paper is in the following form,

$$\mathcal{O}_M^{(\omega)}(\vec{z},t) = \sum_{\vec{y}} \omega(\vec{y})\bar{q}(\vec{z},t)\gamma_M q(\vec{z}+\vec{y},t), \tag{47}$$

where $\omega(\vec{y})$ is a smearing function and $\gamma_M = \gamma_5$ and γ_1 for the pseudoscalar and the vector respectively. Using these mesonic operators I construct the meson correlators $G_M^{\omega' \leftarrow \omega}(t)$ in the Coulomb gauge as the following,

$$G_M^{\omega' \leftarrow \omega}(t) \;=\; \sum_{\vec{z}} \langle \mathcal{O}_M^{(\omega')}(\vec{z},t)\mathcal{O}_M^{(\omega)\dagger}(0)\rangle \tag{48}$$

According to our strategy, I need to construct a good operator which has large overlap with the ground state (or the excited state) of heavy quarkonium. For this purpose I examine two types of correlators.

In the first type of correlator I use the smeared source and point sink ($\omega'(\vec{y}) \propto \delta(\vec{y})$), which is already used in the calibration described in Sect. 3.3 . This source function is defined from the measured wave function $w(\vec{x})$[43] so that the smearing reflects the actual distribution of quark and anti-quark. This smearing procedure works well for the suppressing higher excited state to the correlator. The wave function is well fitted to the form

$$w(\vec{y}) \propto \exp\left(-a|\vec{y}|^p\right). \tag{49}$$

The determined parameters a and p are used to generate the smearing function. These correlators are used in the charmonium spectroscopy in the next subsection.

For the study at $T > 0$ I need more systematic optimization of the correlators. I apply the variational analysis, and regard the diagonalized correlator as the optimized correlator. This analysis can extract not only the ground state but also the excited state. In this analysis I use the correlators with smeared source and sink, whose smearing functions are determined by solving the Schrödinger equation with the potential model. This technique is mentioned in Sect. 4.3 .

4.2 Charmonium spectroscopy

I show the results of spectroscopy for the heavy quarkonium at $T = 0$, which is the basis of the study at $T > 0$. In this section I also examine how our action works in the heavy quark system. The pseudoscalar and the vector meson channels are measured with the parameters listed in Table 6. Figure 12 show the effective mass plot at $T = 0$. In this calculation I use the correlators with the smeared source introduced in the previous

	$1/\kappa$	$m_{\rm Ps}$	$m_{\rm V}$	HFS
	10.300	0.77934(75)	0.79146(83)	0.01213(26)
Set-I	9.868	0.68235(77)	0.69600(88)	0.01365(30)
	9.480	0.59381(78)	0.60917(91)	0.01535(35)
	9.041	0.54170(39)	0.55050(43)	0.00880(15)
Set-II	8.797	0.47236(39)	0.48238(44)	0.01002(16)
	8.590	0.41029(40)	0.42182(45)	0.01152(18)

Table 7: Spectroscopy for Set-I and Set-II with parameters in Table 6. HFS means the hyperfine splitting for a heavy quarkonium, $m_{\rm Ps} - m_{\rm V}$. There results are shown in a_τ unit.

subsection. Here the parameters for the smearing function are $a = 0.7096,\ p = 1.1267$ for Set-I and $a = 0.2978,\ p = 1.1918$ for Set-II. The plateaus of the effective mass appear beyond $t \simeq 10$ (Set-I), 20 (Set-II). Concerning the determination of smearing function our choice works well in heavy quark system. On the other hand in the light quark system the wider smearing function enhances the ground state contribution[29]. In the small t region, contributions from the excited states remain. However this small t region is the main stage of the study at $T > 0$. In order to estimate the temperature effects of the ground state contribution at the high temperature, I need further improvement of the mesonic operator. In the next subsection more systematic study with variational analysis is examined.

I fit the correlator to the single exponential form at $t = 30$–36 (Set-I), 40–48 (Set-II). These results are summarized in Table 7. The parameters with $1/\kappa = 9.868$ (Set-I) and $1/\kappa = 8.797$ (Set-II) in Table 7 correspond approximately to the charm quark. Therefore I study the meson correlators with these parameters in the successive calculations.

Figure 13 shows the hyperfine splitting for charmonium ($m_{J/\psi} - m_{\eta_c}$). For comparison, results of other group are shown simultaneously. Here I notice that these results largely depend on how to determine the lattice cutoff scale. Results of Fermilab action on the isotropic lattice[44], whose scale is determined from the physical value of the string tension, are roughly consistent with our results. Results of heavy relativistic action on anisotropic lattice[33] and NRQCD[45] show the similar tendency. These scales are determined from the Sommer scale and the 1P-1S splitting respectively. However, all the quenched results are roughly a half of experimental results 117(2)MeV[24]. The differences from the experimental value of the hyperfine splitting can be partly explained with the dynamical quark effects[46].

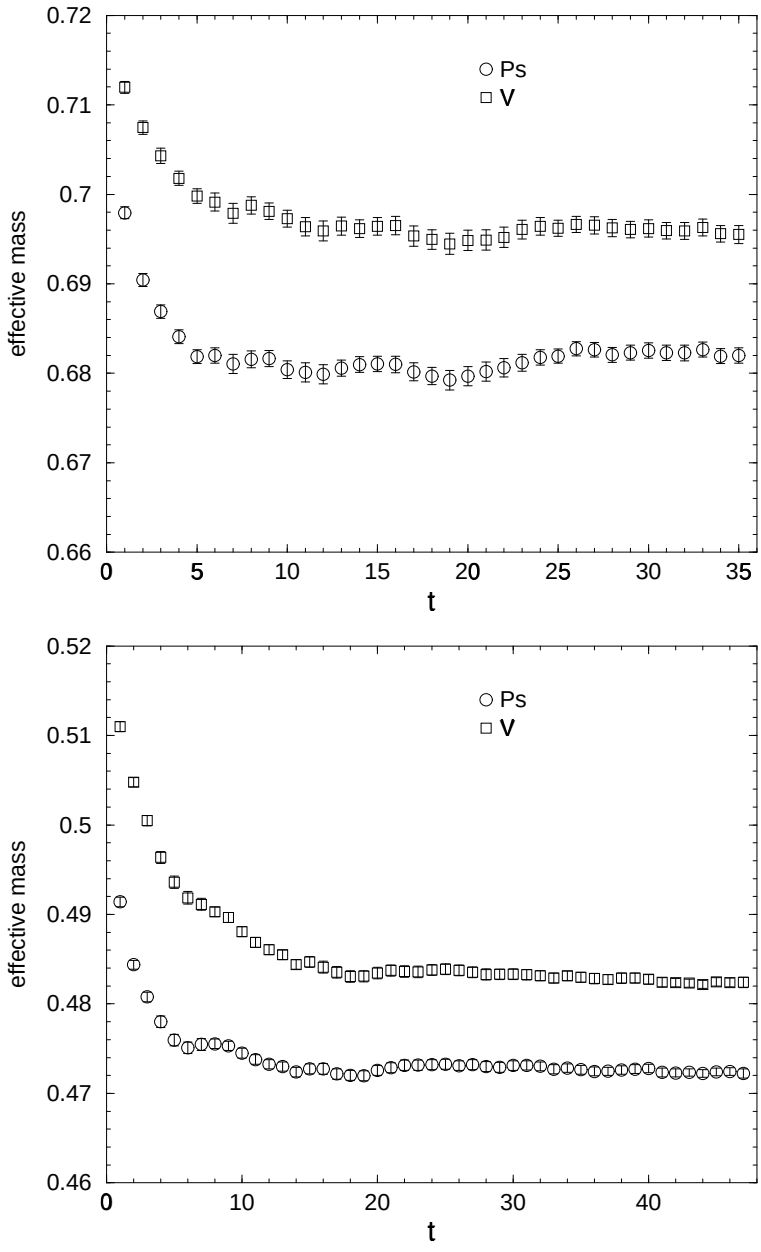

Figure 12: Effective masses at $T = 0$. The top figure is for Set-I and the bottom one is Set-II.

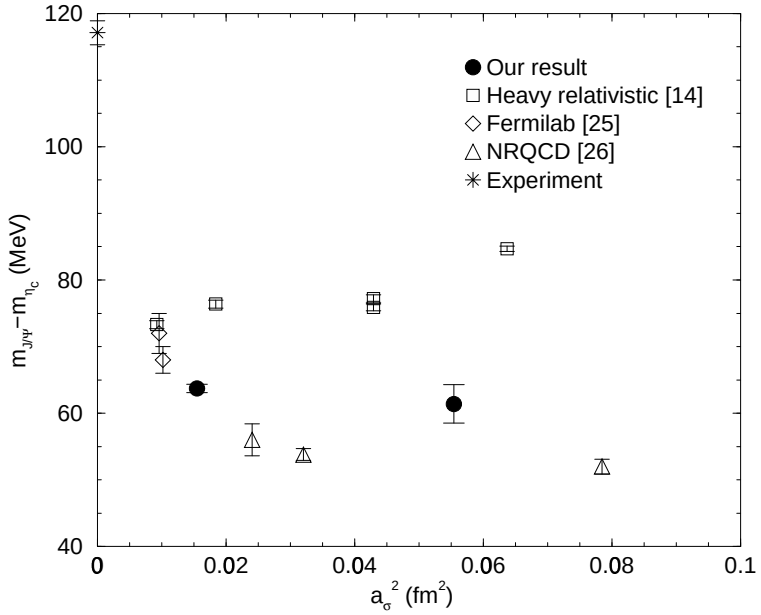

Figure 13: Hyperfine splitting for charmonium. On this figure results of the other group are also shown. These groups[34, 45, 46] used the Sommer scale, the string tension and 1P-1S splitting for the determination of the lattice cutoff scale respectively.

4.3 Variational analysis

I examine the variational analysis for constructing more optimized operators. With this analysis I can construct series of operators which have better matching to the states of interest.

Here I explain the principle of variational analysis briefly. Firstly, I suppose that the state generated by mesonic operator on the lattice is the linear combination of eigenstates for Hamiltonian. Practically I assume that the generated states consist of N linearly independent states. Then I prepare N mesonic operators, which have the same quantum numbers. These operators are constructed with different smearing function $w(\vec{x})$ in Eq.(47). Then I get the $N \times N$ correlator matrix, $C_M^{ij}(t)$, as the following,

$$C_M^{ij}(t) = \sum_{\vec{z}} \langle \mathcal{O}_M^{(\omega_i)}(\vec{z}, t) {\mathcal{O}_M^{(\omega_j)}}^\dagger(0) \rangle. \tag{50}$$

Because of the symmetric nature of this matrix, I can get the diagonalized correlators which are optimized correlators for the state of interest.

In our study this variational analysis is applied in the minimal space including the ground, such as 1st excited and 2nd excited state. I have to prepare the smearing functions so that this analysis works well in this condition. Thus I construct the smearing functions $\phi_l(r)$ using the Schrödinger equation with the potential model,

$$\begin{aligned} \left[-\frac{1}{2m_R}\frac{d^2}{dr^2} + \frac{l(l+1)}{2m_R r^2} + V(r) \right] y_l(r) &= E y_l(r), \\ y_l(r) &= r\phi_l(r), \end{aligned} \tag{51}$$

where $V(r)$ is the static quark potential measured on our lattice and $m_R = 1.5/2$ GeV. The spin interaction is neglected and I calculate only S-state ($l = 0$). Figure 14 shows the lowest three solutions $\phi_0(r)$ and the measured wave function at $T = 0$ for Set-II.

I calculate the diagonalized correlator using the three types of smearing function in Fig. 14. The orthogonal matrices are obtained at each t, then I adopt the averaged one as the orthogonal matrix which is used for the calculation of the diagonalized correlator, which is shown in Fig. 15 and 16.

With the orthogonal matrix I obtain the diagonalized correlator. Then its effective mass plots are shown in Fig. 17 and 18. I fit the these data at $t = 10$–36 for Set-I and $t = 14$–48 for Set-II, and get the results summarized in Table 8.

The extracted mass of 1S state are consistent with previous results in Table 7. In the Table 8 results are presented in a_τ unit and physical unit for each sets, where the latter case includes the error of a_τ.

The results of 2S-1S splitting are consistent with the experimental values within a statistical error. This is in contrast to the case of the hyperfine splitting in which I

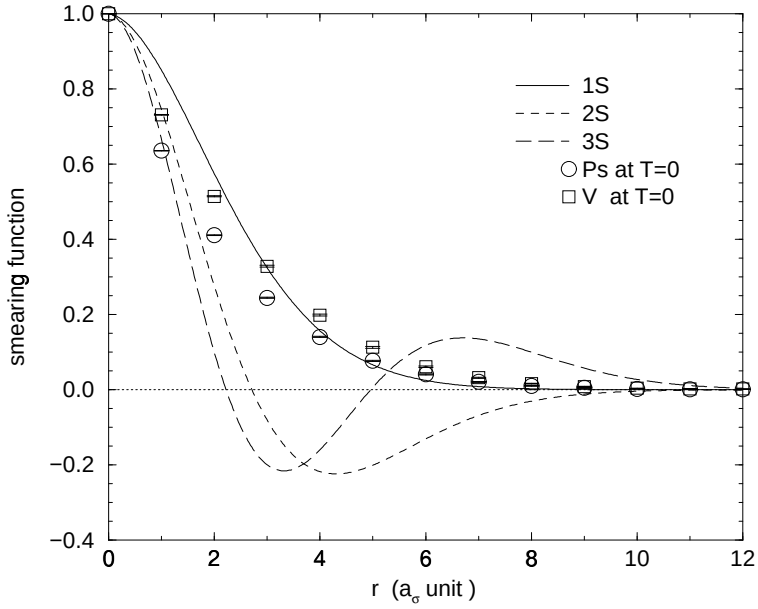

Figure 14: Smearing functions for the variational analysis for Set-II. These are calculated with the Schrödinger equation with the potential model. The circle and square symbols are the wave function measured on the lattice at $T = 0$ for the pseudoscalar and the vector respectively.

obtain the half of the experimental value, 2S-1S splitting is in good agreement with experimental value.

The variational analysis can directly extract one of correlators for the ground and excited states. Therefore this analysis is useful to investigate the excited state of hadron. In the next section I mainly use this analysis at $T > 0$.

	Ps(2S)	V(2S)	$m_{\mathrm{Ps(2S)}} - m_{\mathrm{Ps(1S)}}$	$m_{\mathrm{V(2S)}} - m_{\mathrm{V(1S)}}$
Set-I	0.7688(34)	0.7794(38)	0.0868(30)	0.0848(33)
(MeV)	3460(155)	3507(157)	391(22)	382(23)
Set-II	0.5641(66)	0.5696(73)	0.0913(64)	0.0869(70)
(MeV)	3587(55)	3622(58)	581(41)	553(45)
Exp. value (MeV) [24]	3594(5)	3685.96(9)	614(5)	589.07(13)

Table 8: Spectroscopy for 2S state and 2S-1S splitting of charmonium. For each sets the upper values are in a_τ unit and the lower one are in physical unit. The error in physical unit includes the error of a_τ.

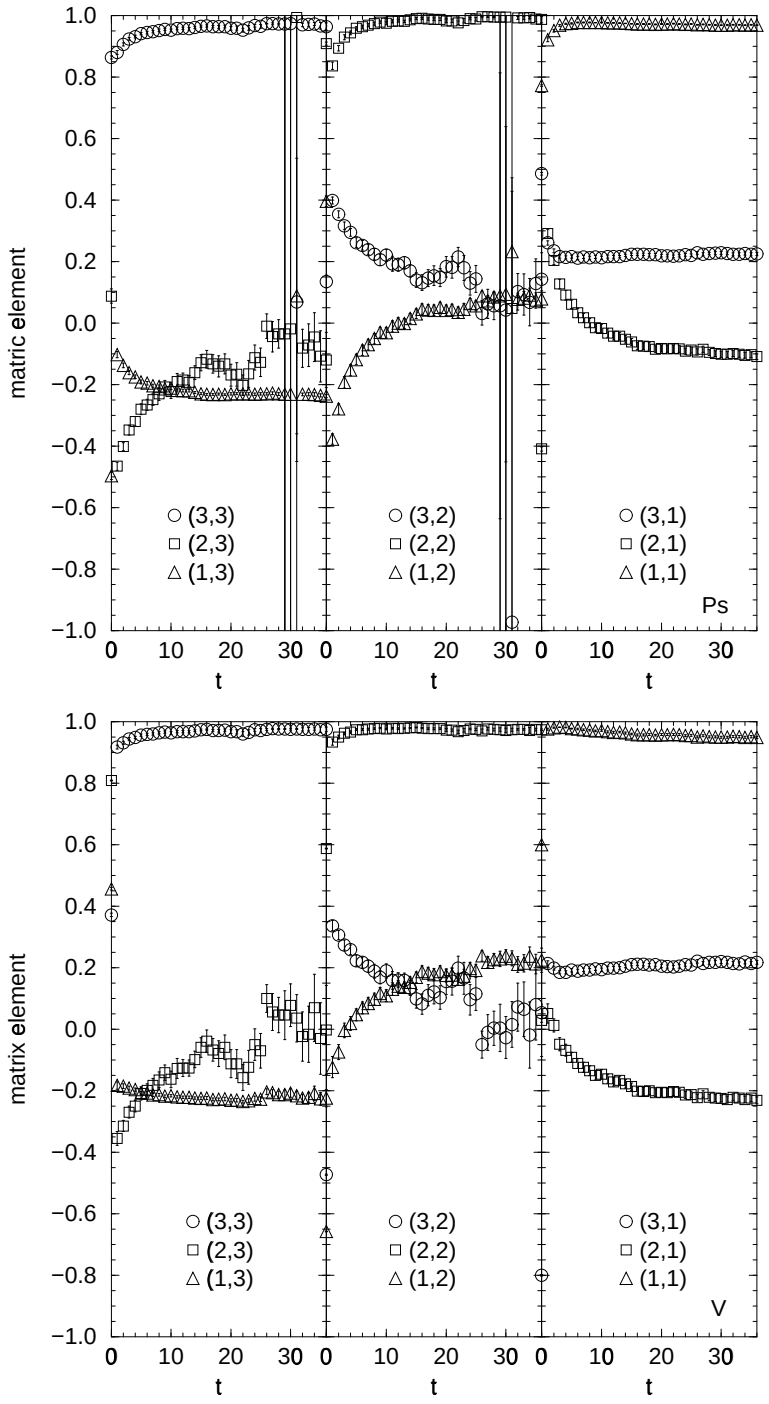

Figure 15: The results of orthogonal matrix elements for Set-I. The top figure is the result of pseudoscalar meson and the bottom one is that of vector meson.

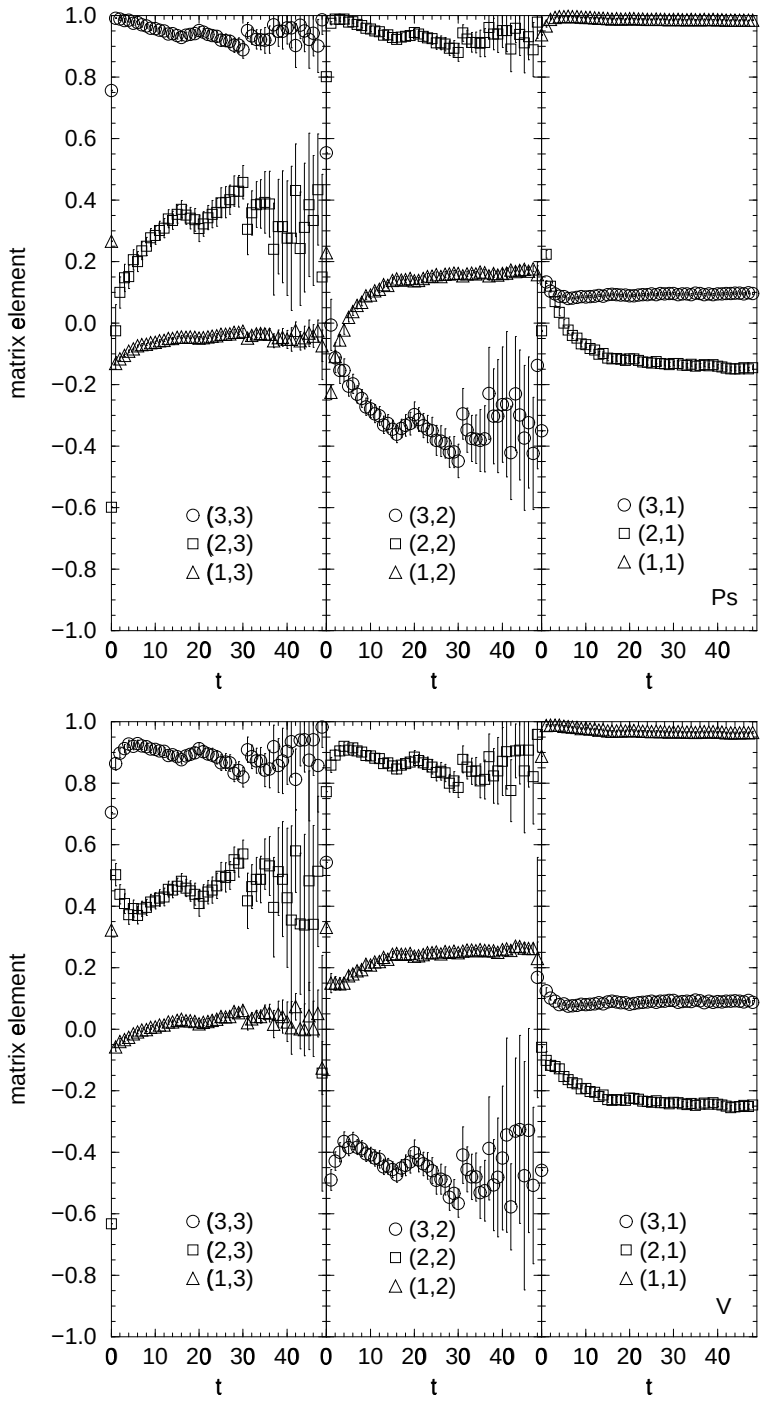

Figure 16: The results of orthogonal matrix elements for Set-I. The top figure is the result of pseudoscalar meson and the bottom one is that of vector meson.

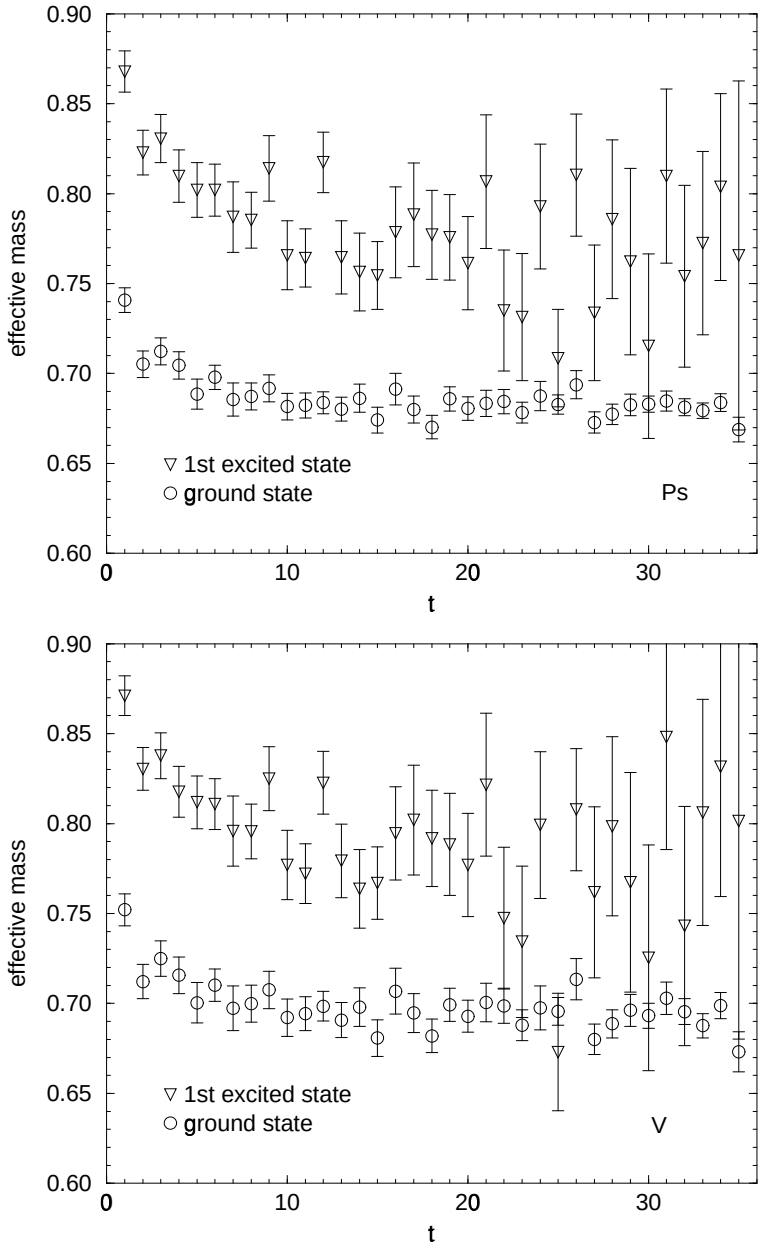

Figure 17: Effective mass of diagonalized correlator for Set-I at $T = 0$. The top figure is the result of pseudoscalar meson and the bottom one is that of vector meson. Only ground and 1st excited one are shown because of the large noise for the 2nd excited state.

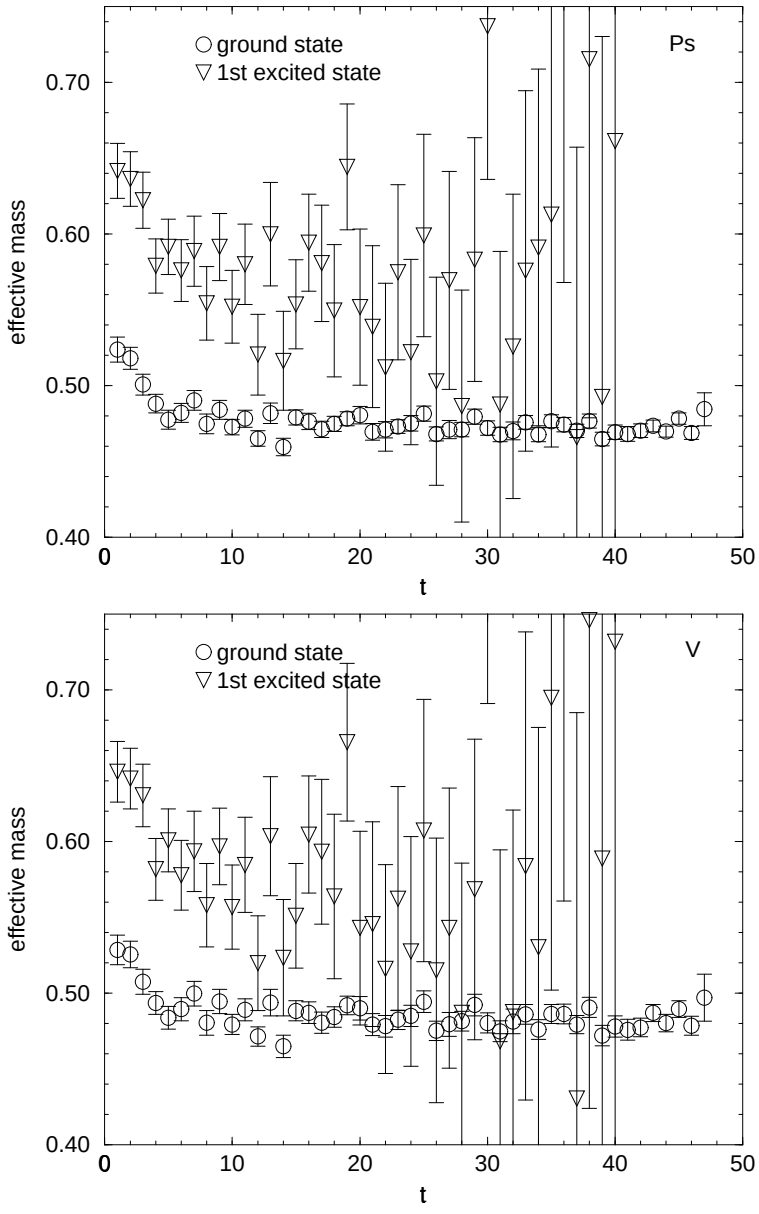

Figure 18: The same figure as Fig. 17 for Set-II.

5 Results at Finite temperature

5.1 Temperature dependence of correlators

In accordance with our strategy the optimized operators which are constructed at $T = 0$ are applied to the case at $T > 0$. The optimized operators are defined from the variational analysis in the previous section. I construct the correlator matrix at $T > 0$ with the same basis (smearing function) as $T = 0$ (Fig. 14). Then the orthogonal matrix defined at $T = 0$ are operated to this correlator matrix, and its diagonal correlators are discussed in this subsection. Here I call these correlators as $C_1(t)$, $C_2(t)$ and $C_3(t)$ in the order of their effective masses. Figure 19 and 20 show the effective masses of $C_1(t)$ and $C_2(t)$, although the effective mass of $C_3(t)$ is too noisy.

Below T_c ($N_t = 26$) I can find the plateau of effective mass. The ground and the excited states seem to be observed below T_c. The masses of these states are almost the same as $T = 0$ or slightly larger. Therefore I conclude that these correlators have little thermal effects at this temperature, and the spectral structure seems to keep the form at $T = 0$. However it is difficult to identify the plateau precisely and determine the mass quantitatively with the present statistics. More detailed analysis with higher statistics may open a stage to discuss the potential mass shift of charmonium near to the T_c[10].

Above T_c ($N_t = 22$ and 16) effective masses have no clear plateau in whole t region. These behaviors at least signal significant change of correlators when the system crosses T_c. This behavior appears noticeably in the effective mass of $C_2(t)$. In the case of the light quark system investigated in the Ref. [29], the effective masses increase as T in the pseudoscalar and the vector channels. The observed behavior in present work, however, shows qualitatively different nature of the correlators.

As the comparison with above results, Fig. 21 shows the effective mass plots at $T > 0$ for the correlators with smeared source by the wave function and point sink, described in Sect. 4.1 .

These results are consistent with the variational analysis. The remarkable change in the vector channel is apparently seen. Then the order of effective masses for the pseudoscalar and the vector mesons is reversed above T_c, the same as the case of free quark. This phenomenon is also brought about in the system of light quarks[29].

From the results of this subsection, I observed that the temporal mesonic correlators change drastically when the system goes through the deconfining transition. I can consider the several pictures which can explain (consistent with) the change for correlators. One of these pictures is that the mesonic bound state disappear in the deconfinement phase. This is the most interesting case as stated in our motivations. In order to discuss this picture I investigate the correlation between c and $\bar{c}$ in the next subsection.

5.2 Wave function

In this subsection the $c\bar{c}$ bound state at $T > 0$, especially in the deconfinement phase, is discussed in the light of "wave function". The definition of the "wave function" in the Coulomb gauge is as follows.

$$w_M(\vec{r}, t) = \sum_{\vec{x}} \langle \bar{q}(\vec{x} + \vec{r}, t) \gamma_M q(\vec{x}, t) \mathcal{O}_M^\dagger(0) \rangle \tag{52}$$

Here this definition is the same form as the wave function at $T = 0$. This wave function shows the spatial correlation between q and $\bar{q}$, and gives us a hint of the mesonic bound state from its t dependence. In the case of free quarks, $q\bar{q}$ has no bound state, then the wave function ought to broaden with t. On the other hand suppose quark and anti-quark form a bound state, the wave function holds the stable shape with t. I can discuss the existence of such the bound state by observing the t-dependence of the wave function. For this purpose I compare the correlation at spatial origin with another spatially separated point at each t. Therefore I define the wave function normalized at the spatial origin, $\phi_M(\vec{r}, t)$, as follows,

$$\phi_M(\vec{r}, t) = \frac{w_M(\vec{r}, t)}{w_M(\vec{0}, t)}. \tag{53}$$

From now on the wave function denotes this normalized definition.

Since the question is whether wave function has a stable shape or not, it is not necessary to use the optimized operator. Therefore the smeared source function with exponential form defined as with Eq.(49), is used for the analysis of t-dependence of the wave function. Fig. 22 shows the results at $T > 0$ with the smeared source function which is slightly wider than the observed wave function at $T = 0$. The wave functions composed of free quark propagators are also shown together.

As is shown in the Fig. 22, the behaviors of the observed wave functions are clearly different from that of the free quark case at each temperature and in each mesonic channel. In the free quark case the wave functions are broadening as t as expected. On the other hand, the observed wave functions are stable with the slightly narrower shape than source function. These behaviors are independent of the source function.

For a visible expression, I define the averaged orbital radius, r_0, as

$$r_0^3(t) = \sum_z 3z^2 \phi_M(z, t), \tag{54}$$

where I suppose a spherical symmetric wave function and the sum is over z axis. These $r_0(t)$ of Set-I and Set-II are shown in Fig. 23. Figure 23 shows the t dependence of r_0 in the physical unit, where the error estimation takes into account the error of a_σ and a_τ. These results for Set-I and II are roughly consistent with each other. The behavior of

observed r_0 are obviously different from free quark case, and shows the stable behavior with respect to t. This asymptotic value for the vector channel is larger than that of the pseudoscalar.

Below T_c, r_0 for each channel are almost same as the case of $T = 0$. At $T \simeq 1.5T_c$ the observed r_0 are slightly larger than that of $T < T_c$. However the wave function, even in the deconfinement phase, seem to have the stable r_0 independently of the source function. Therefore I conclude the same strong spatial correlation as below T_c survives in the deconfinement phase at each mesonic channel.

The results of this subsection seem to suggest the presence of the hadronic state in the deconfinement phase, at least up to $1.5T_c$. This is the opposite situation to the picture mentioned in the previous subsection.

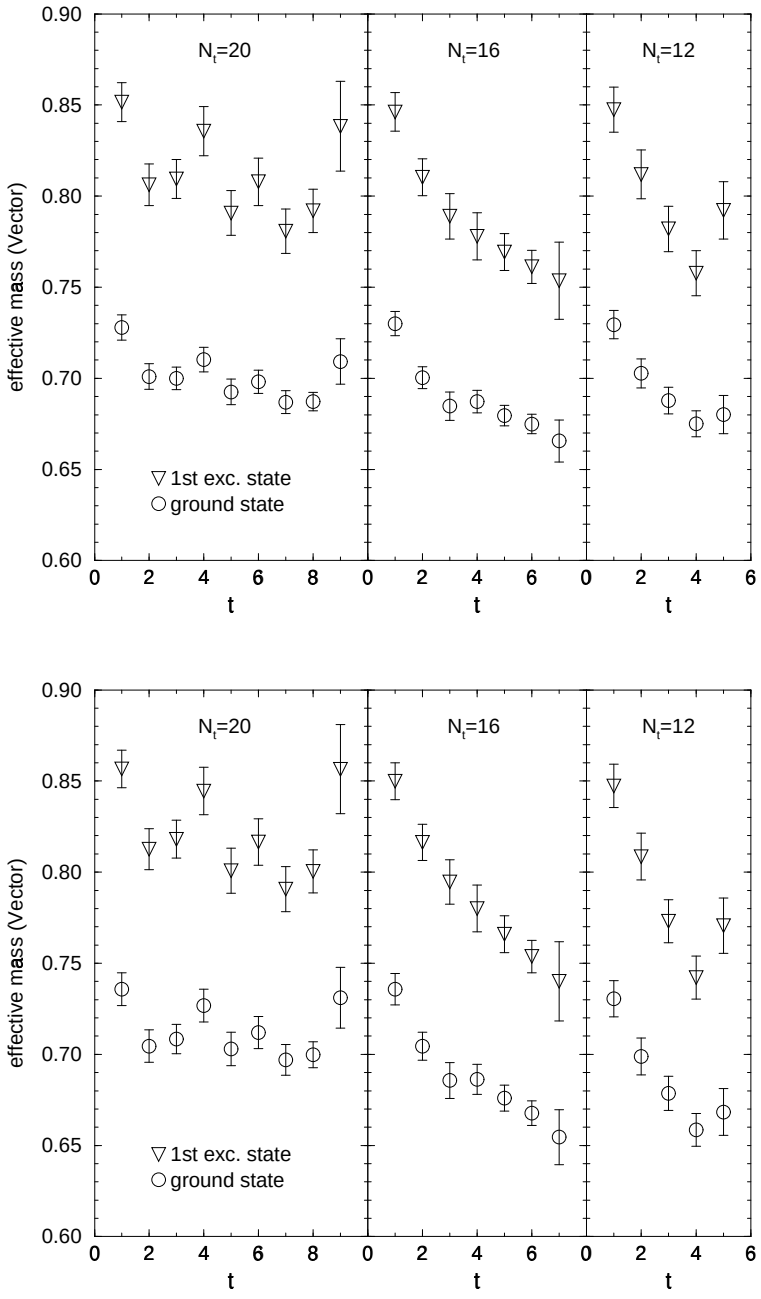

Figure 19: Effective mass of diagonalized correlator for Set-I at $T > 0$. Orthogonal matrix at $T = 0$ are used for diagonalization. The top figure is the result of the pseudoscalar meson and the bottom one is that of the vector meson. Because of the large noises only the lowest two effective masses are shown.

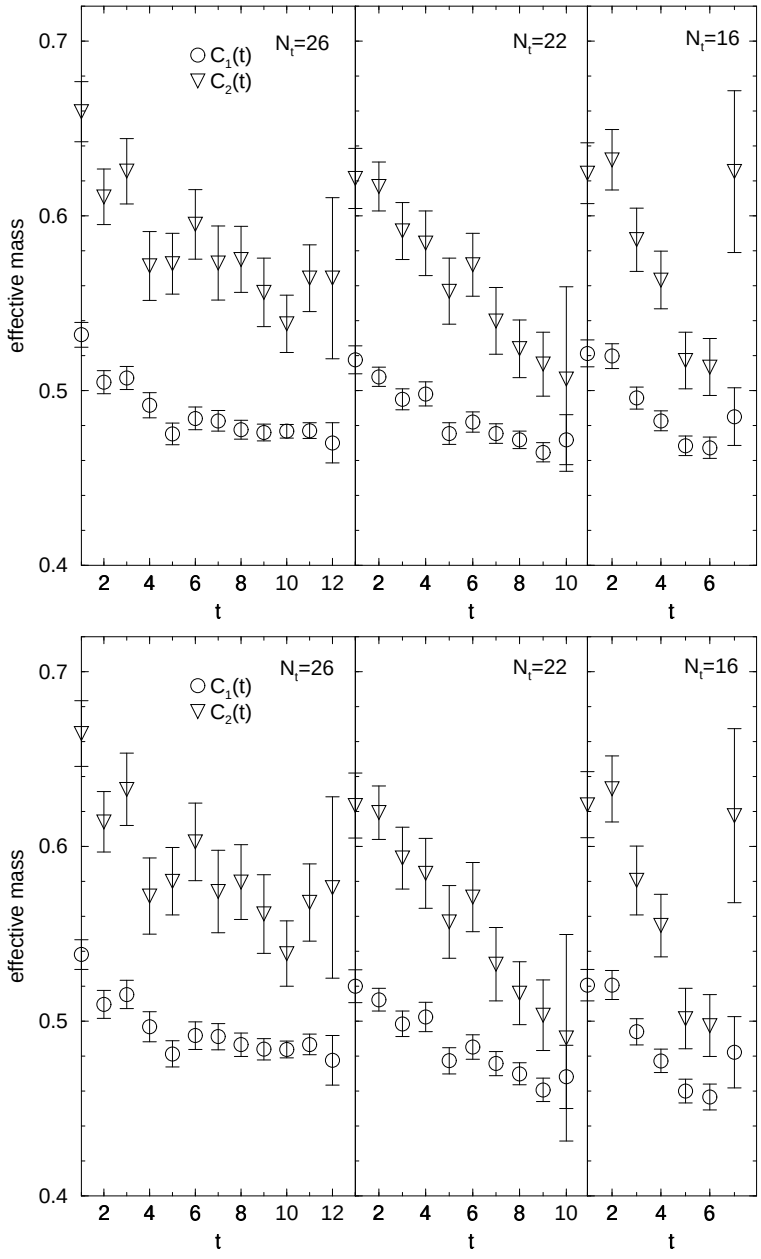

Figure 20: Effective mass of diagonalized correlator for Set-II at $T > 0$. Orthogonal matrix at $T = 0$ are used for diagonalization. The top figure is the result of the pseudoscalar meson and the bottom one is that of the vector meson. Because of the large noises only the lowest two effective masses are shown.

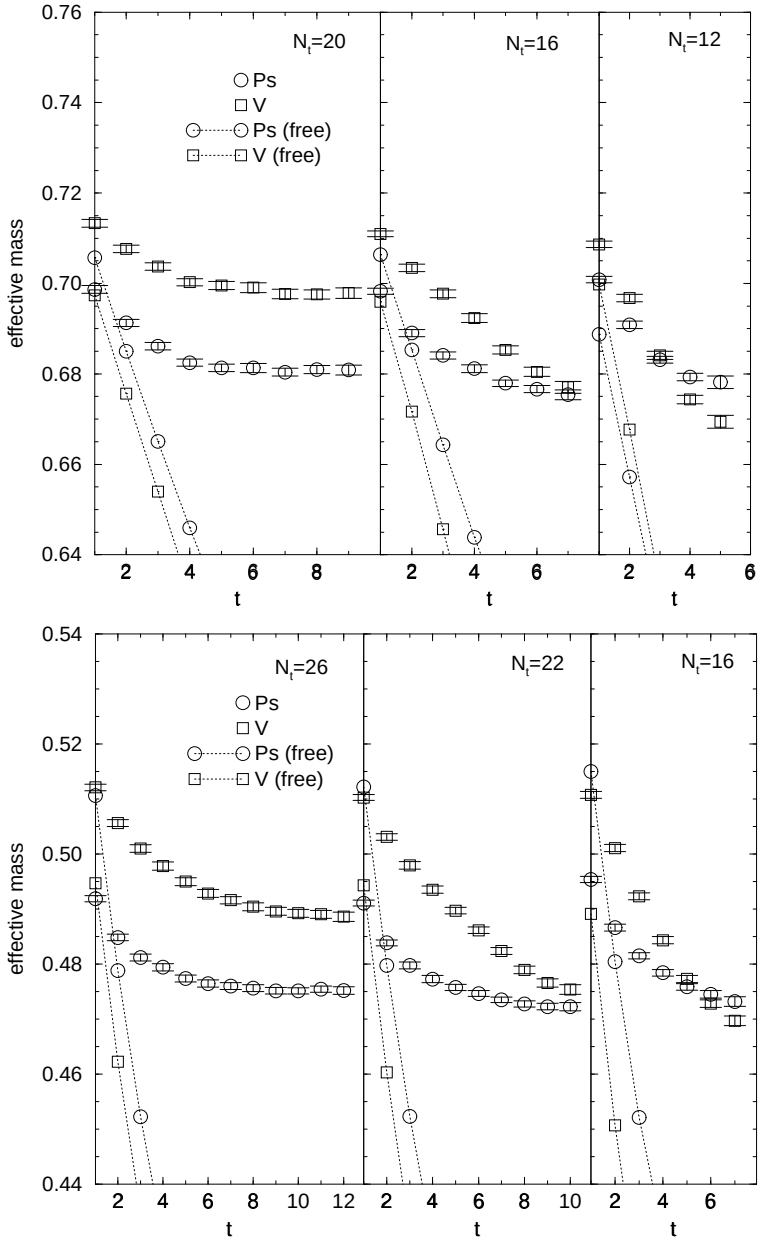

Figure 21: Effective masses at $T > 0$. The top figure is that of Set-I and the bottom one is Set-II. In the figures of Set-I, $N_t = 20, 16$ and 12 correspond to $T/T_c \simeq 0.93, 1.15$ and 1.5 respectively. In the figures of Set-II, $N_t = 26, 22$ and 16 are $T/T_c = 0.93, 1.10$ and 1.53. The symbols with dotted lines show the case of free quarks.

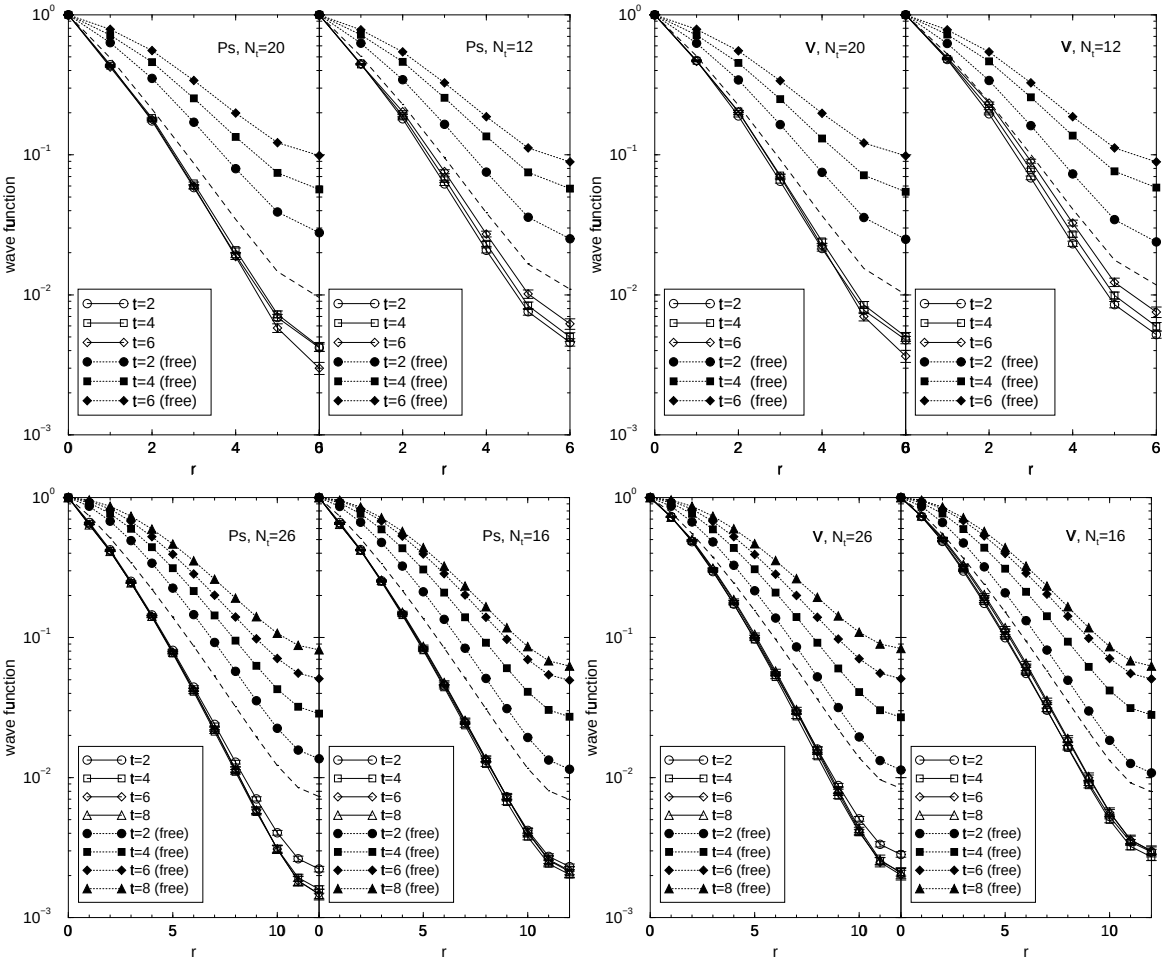

Figure 22: The results of "wave function" : dotted lines (full symbols) show free quark case, and dashed line (no symbol) show the initial shape of "wave function" i.e. shape of source function. The different symbols correspond to the different t step. The result of pseudoscalar is left one, and that of vector is the other. The top figures are for Set-I and the bottom ones are for Set-II.

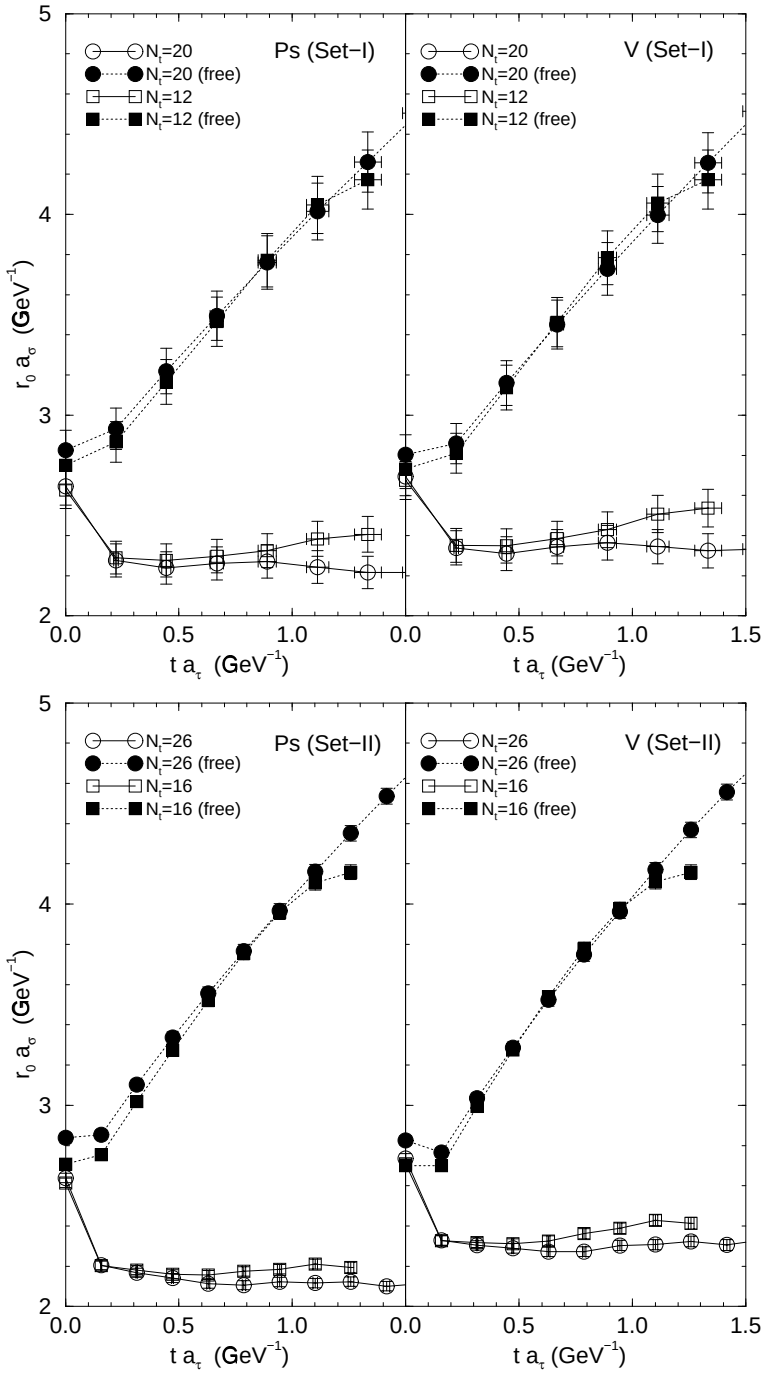

Figure 23: t dependence of r_0. The top figure is for Set-I and the bottom one is for Set-II.

6 Conclusion

In this paper I explored the charmonium correlators in the Euclidean temporal direction at $T > 0$ using the quenched lattice QCD simulation. The high resolution in the temporal direction is achieved by employing the anisotropic lattice. I examined the thermal effect on the correlators based on the following two quantities: the correlators between the optimized operators tuned at $T = 0$, and the t-dependence of $q\bar{q}$ wave function.

In the calculation of the wave function in the Coulomb gauge, I found the strong spatial correlation even above T_c, up to at least $1.5T_c$. These results indicate the quark and the anti-quark tend to be close each other even in the deconfinement phase. The similar result is reported in the light quark mass region in the Ref. [29]. In the case of charm quark mass these results suggest that the J/ψ may not easily be resolved until $\sim 1.5T_c$. On the other hand, I also observed significant change of the nature of the correlators between the operators optimized at $T = 0$. This was signaled by the drastic change of the behavior of effective mass. This situation is interesting, and at the same time puzzling. It is possible to consider several pictures which are able to explain our results. For example, the mesonic spectral function still have some peaks above T_c, and its width are broadened with thermal effects. Such a situation naturally explains the observed results in this work. The existence of hadronic modes just above T_c were also suggested by the previous works[26]. From the analysis of temporal meson correlators at $T > 0$, the QCD vacuum still has non-perturbative nature above the phase transition, and far from the perturbative plasma state of quark and gluon. In spite of several systematic uncertainties our results in the present work have important and interesting implications on the fate of hadronic states above the critical temperature.

Our approach is directly applicable to the dynamical configuration. If the full QCD simulation on the anisotropic lattice is appropriately implemented. Then it is interesting to investigate what effect our results receive from the dynamical quarks. To achieve the high resolution in the temporal direction, I adopted the anisotropic lattice and employed the O(a) improved Wilson quark action on it. These implementation also useful to study the heavy particle such as the glueballs[47] and scalar mesons. For the correlators of these states I are inevitably forced to extract the signals at the short time separation. The large temporal lattice cutoff enables us to simulate the heavy particles on lattices of moderate size with keeping the finite lattice cutoff effect small. The detailed information in the temporal direction is also significantly useful for the direct extraction of the spectral function from the lattice data. This approach may give us the further information on the spectral structure of mesons at $T > 0$.

7 Acknowledgments

I would like to thank to all of the colleagues from the QCD-TARO Collaboration for the suggestions and supports.

I thank H. Matsufuru for the great support and useful discussion. R. Katayama supports my numerical simulation. I especially thank to Prof. O. Miyamura and Prof. A. Nakamura, they guide me to the completion of this thesis with their great advice.

I am greatful to K. Hayashi and other members of the Hadron physics laboratory for their encouragement and kindly help. T.Onogi, N.Nakajima and J.Harada give me the good advice for this thesis.

The simulation has been done on Intel Paragon XP/S and NEC HSP at the Institute for Nonlinear Science and Applied Mathematics, Hiroshima University, NEC SX-4 at Research Center for Nuclear Physics, Osaka University and Hitachi SR8000 at KEK.

References

[1] M. Gell-Mann, *Phys. Lett.* **8** (1964) 214.

[2] G. Zweig, Preprints CERN-TH 401 and 412 (1964).

[3] U. Heinz, P. R. Subramanian and W. Greiner, *Z. Phys.* **A318** (1994) 247.

[4] P. Koch, B. Müller, H. Stöker and W. Greiner, *Mod. Phys. Lett.* **A3** (1988) 737.

[5] J. Ellis, U. Heinz and H. Kowalski, *Phys. Lett.* **B233**, (1989) 233.

[6] K. S. Lee, M. J. Rhoades-Brown and U. Heinz, *Phys. Rev.* **C37** (1988) 1452.

[7] C. Greiner, P. Koch and H. Stöker, *Phys. Rev. Lett.* **58** (1987) 1825.

[8] T. Hatsuda and S. H. Lee, *Phys. Rev.* **C46** (1992) 34.

[9] T. Hatsuda and H. Shiomi, *Nucl. Phys.* **A590** (1995) 103c.

[10] T. Hashimoto, O. Miyamura, K. Hirose and T. Kanki, *Phys. Rev. Lett.* **57** (1986) 2123.

[11] T. Matsui and H. Satz, *Phys. Lett.* **B178** (1986) 416.

[12] For a recent review, see, F. Karsch, *Nucl. Phys.* (Proc. Suppl.) **B83-84** (2000) 14.

[13] For a recent review, see, S. Ejiri, hep-lat/0011006, Proceedings of the Lattice2000.

[14] B. Beinlich et al., *Eur. Phys. J.* **C6** (1999) 133.

[15] M. Okamoto et al. (CP-PACS Collaboration), *Phys. Rev.* **D60** (1999) 094510.

[16] A. Ali Khan et al. (CP-PACS Collaboration), hep-lat/0008011.

[17] F. Karsch et al., hep-lat/0010040, Proceedings of the Lattice2000.

[18] T. Takaishi and Ph. de Forcrand,hep-lat/0011003, Proceedings of the Lattice2000.

[19] C. Bernard et al., *Phys. Rev.* **D55** (1997) 6861.

[20] T. DeGrand and C. DeTar, *Phys. Rev.* **D34** (1986) 2469.

[21] C. DeTar and J. Kogut, *Phys. Rev. Lett.* **59** (1987) 399.

[22] F. Karsch et al. (MT_c Collaboration), *Phys. Rev. Lett.* **67** (1991) 302.

[23] NA50 Collaboration, *Phys. Lett.* **B477** (2000) 28.

[24] D.E. Groom et al.(Particle Data Group), *Eur. Phys. Jour.* **C15** (2000) 1.

[25] For recent review, see e.g. H. Meyer-Ortmanns, *Rev. Mod. Phys.* **68** (1996) 473.

[26] C. DeTar, *Phys. Rev.* **D32** (1985) 276; **D37** (1988) 2328.

[27] T. Hatsuda and T. Kunihiro, *Phys. Rep.* **247** (1994) 221.

[28] C. DeTar and J.B. Kogut, *Phys. Rev.* **D36** (1987) 2828.

[29] Ph. de Forcrand et al. (QCD-TARO Collaboration), *Phys. Rev.* **D63** (2001) 054501.

[30] A. El-Khadra, A. S. Kronfeld and P. B. Mackenzie, *Phys. Rev.* **D55** (1997) 3933.

[31] B. Sheikholeslami and R. Wohlert, *Nucl. Phys.* **B259** (1985) 572.

[32] T. R. Klassen, *Nucl. Phys.* (Proc. Suppl.) **B73** (1999) 918.

[33] P. Chen, hep-lat/0006019.

[34] A. Ali Khan, et al (CP-PACS Collaboration), hep-lat/0011005

[35] G. P. Lepage and P. B. Mackenzie, *Phys. Rev.* **D48** (1993) 2250.

[36] B.A. Thacker and G. P. Lepage, *Phys. Rev.* **D43** (1991) 196.

[37] F. Karsch, *Nucl. Phys.* **B205** (1982) 285.

[38] M. Lüscher and P. Weisz, *Commun. Math. Phys.* **97** (1985) 59; Erratum *Commun. Math. Phys.* **98** (1985) 433.

[39] M. Fujisaki et al. (QCD-TARO Collaboration), *Nucl. Phys.* (Proc. Suppl.) **B53** (1997) 426.

[40] J. Engels, F. Karsch and T. Scheideler, *Nucl. Phys.* (Proc. Suppl.) **B63** (1998) 427.

[41] T. R. Klassen, *Nucl. Phys.* **B533** (1998) 557.

[42] E. Eichten et al, *Phys. Rev.* **D21** (1980) 203.

[43] C. Bernard et al, *Phys. Rev. Lett.* **68** (1992) 2125.

[44] P. Boyle (UKQCD Collaboration), hep-lat/9903017.

[45] N. H. Shakespeare and H. D. Trottier, *Phys. Rev.* **D58** (1998) 034502.

[46] A. El-Khadra, *Nucl. Phys.* (Proc. Suppl.) **B30** (1993) 449.

[47] C. J. Morningstar, M. Peardon, *Phys. Rev.* **D56** (1997) 4043.

[48] G. S. Bali and K. Schilling, *Phys. Rev.* **D46** (1996) 2636.

[49] A. M. Ferrenberg and R. H. Swendsen, *Phys.Rev.Lett.* **61** (1988) 2635 ; **63** (1989) 1195.